

Feature Based Qualification (FBQ) of Wire Arc Additively Manufactured (WAAM) 17-4PH Martensitic Stainless Steels

Pavan Ajjarapu
Yukinori Yamamoto
William Carter
Andrzej Nycz
Soumya Nag
Jeffrey Burdick

September 2024

DOCUMENT AVAILABILITY

Online Access: US Department of Energy (DOE) reports produced after 1991 and a growing number of pre-1991 documents are available free via <https://www.osti.gov>.

The public may also search the National Technical Information Service's [National Technical Reports Library \(NTRL\)](#) for reports not available in digital format.

DOE and DOE contractors should contact DOE's Office of Scientific and Technical Information (OSTI) for reports not currently available in digital format:

US Department of Energy
Office of Scientific and Technical Information
PO Box 62
Oak Ridge, TN 37831-0062
Telephone: (865) 576-8401
Fax: (865) 576-5728
Email: reports@osti.gov
Website: www.osti.gov

This report was prepared as an account of work sponsored by an agency of the United States Government. Neither the United States Government nor any agency thereof, nor any of their employees, makes any warranty, express or implied, or assumes any legal liability or responsibility for the accuracy, completeness, or usefulness of any information, apparatus, product, or process disclosed, or represents that its use would not infringe privately owned rights. Reference herein to any specific commercial product, process, or service by trade name, trademark, manufacturer, or otherwise, does not necessarily constitute or imply its endorsement, recommendation, or favoring by the United States Government or any agency thereof. The views and opinions of authors expressed herein do not necessarily state or reflect those of the United States Government or any agency thereof.

Materials Science and Technology Division
Oak Ridge National Laboratory

**FEATURE BASED QUALIFICATION (FBQ) OF
WIRE ARC ADDITIVELY MANUFACTURED (WAAM) 17-4PH MARTENSITIC
STAINLESS STEELS**

Pavan Ajjarapu
Yukinori Yamamoto
William Carter
Andrzej Nycz
Soumya Nag
Jeff Burdick

September 2024

Prepared by
OAK RIDGE NATIONAL LABORATORY
Oak Ridge, TN 37831
managed by
UT-BATTELLE LLC
for the
US DEPARTMENT OF ENERGY
under contract DE-AC05-00OR22725

CONTENTS

ABSTRACT	4
1. INTRODUCTION	4
1.1 Wire Arc Additive Manufacturing (WAAM):	5
1.2 Complexities & Challenges with WAAM	7
2. PRECIPITATION HARDENED (PH) MARTENSITIC STAINLESS STEEL:	9
2.1 Martensitic Phase Transformation in 17-4PH Stainless Steel	10
2.2 Predictive Phase Diagrams in PH Steels	13
2.3 Heat Treatment for Strengthening 17-4PH Stainless Steel	16
2.4 Welding 17-4PH Stainless Steel: Past Literature	17
2.5 Wire Arc Additive Manufacturing (WAAM) of 17-4PH Stainless Steel	19
3. QUALIFICATION OF METAL ADDITIVE MANUFACTURED (M-AM) PARTS:.....	29
4. CONCLUSION	34
REFERENCES:	34

ABSTRACT

The Department of Defense (DOD) programs of records desire to reduce the time and cost of the development and delivery loop in metal additive manufacturing (AM), including establishing forwarded AM capabilities. The success of these efforts relies on a robust and qualified process. To achieve this, the United States Army Combat Capabilities Development Command Ground Vehicle Systems Center Materials Engineering (GVME) needs to be able to quickly evaluate, test, and develop feedstocks, processes, and parts. This report is directed towards demonstrating the need for a framework for metal AM processes, defining and exploring geometries for metal AM process qualification, testing resultant deposition, and delivering actionable data.

1. INTRODUCTION

The advent of additive manufacturing (AM) has revolutionized fabrication of complex parts for structural applications across many industries, including aerospace, automotive, biomedical, defense, and nuclear [1, 2]. Compared to conventional manufacturing methods, the layer-by-layer and track-by-track strategy of additive manufacturing (AM) processes enables the production of intricate near-net-shaped structures, resulting in cost and time saving [3-8]. Metal additive manufacturing (M-AM) in particular, emerged as a viable option for high-value industrial applications. M-AM involves layer-by-layer metal deposition using a heat source (laser, electron beam, electric arc, etc.), to achieve a desired shape [9]. M-AM can further be classified based on form of feedstock (wire or powder), feedstock feeding mechanism (powder bed or blown powder), and heat source (laser, electron beam, or electric arc), as shown in *Figure 1* [10]. Each type of M-AM has its own unique characteristics. Selective laser melting (SLM) can produce components with near-net shape, while the electron beam melting (EBM) process is better suited for small-sized parts with highly complex designs [9]. Laser powder bed fusion (LPBF) and laser powder directed energy deposition (LP-DED) are the most well-known laser-based processes that have been studied extensively in the literature [11]. On the other hand, wire arc additive manufacturing (WAAM) has been gaining increasing popularity due to its ability to manufacture large-scale metal components at high speeds [4, 5, 9, 12-16].

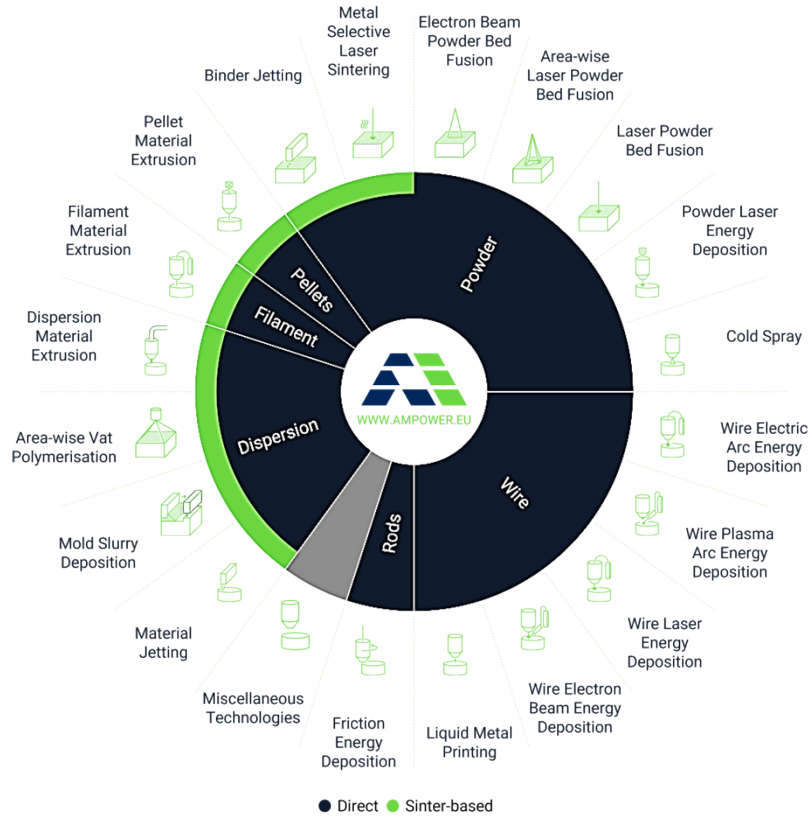


Figure 1: Metal Additive Manufacturing technologies classified according to feedstock type [10]

1.1 WIRE ARC ADDITIVE MANUFACTURING (WAAM):

WAAM technique involves the use of wire as a feedstock material and electric arc as the heating source. Various power sources can be used including as tungsten inert gas, a plasma arc with a transferred arc, and gas metal arc welding (GMAW) [16]. In this process, the wire undergoes heating and melting before being transferred to the melt pool, which then solidifies at the boundary of the melt pool, allowing for the formation of the designed parts layer by layer as depicted in **Figure 2(a)** [4, 17, 18]. WAAM process can be accomplished using various welding techniques such as gas metal arc welding (GMAW), gas tungsten arc welding (GTAW), plasma arc welding (PAW), or cold metal transfer welding (CMT). These methods involve melting metal wires and building a 3D component layer by layer [4, 19-22].

Figure 2(b,c,d) displays a schematic diagram illustrating the GMAW, GTAW, and PAW processes. In GMAW an electric arc is created between a wire electrode that can be consumed and the metal being worked on, where wire is typically oriented at a right angle to the substrate. The GMAW process has four main ways of metal transfer: globular, short-circuiting, spray, and pulsed-spray [23]. Cold metal transfer (CMT) is a modified variation of gas metal arc welding (GMAW) that utilizes a controlled dip transfer mode mechanism and has been extensively utilized in additive manufacturing (AM) processes due to its high deposition rate and low heat input capabilities [24-27]. GTAW and PAW on the other hand, utilize a non-consumable tungsten electrode to generate

the weld where the wire feed orientation can be adjusted (unlike in GMAW) [23]. The plasma arc's high temperature zone is more constricted compared to the GTAW's arc, leading to the deposition of significantly narrower weld beads [28]. The arc energy in PAW can reach up to three times that of GTAW welding, resulting in reduced weld distortion and smaller welds that can be made at greater welding speeds [29-31].

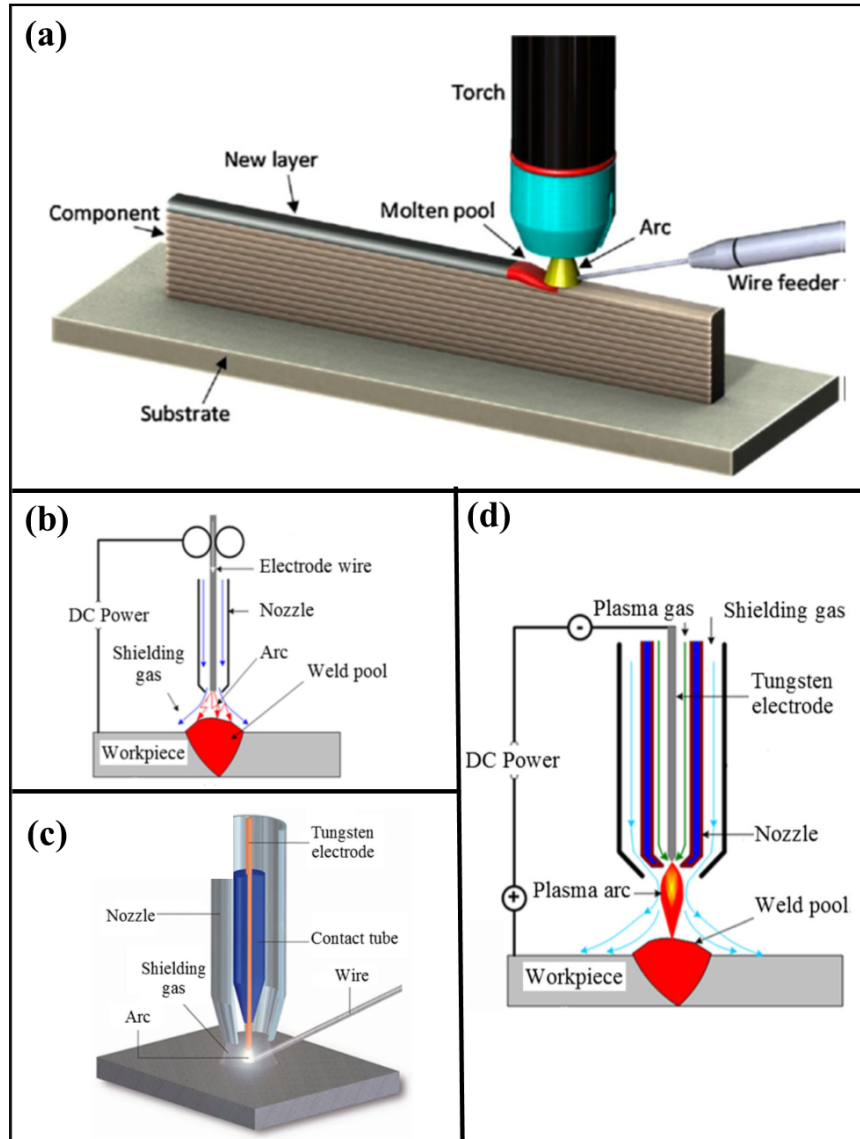


Figure 2: (a) Schematic of WAAM process [18] (b) GMAW (c) GTAW, and (d) PAW process [23]

WAAM offers several advantages compared to other metal additive manufacturing technologies. These include high deposition rates, low investment and operation costs, and broad choice of processable materials. Compared to traditional manufacturing methods, WAAM offers the ability to fabricate medium to large-sized components at high deposition rates, resulting in reduced material waste. Additionally, WAAM is cost-effective in terms of both feedstock and capital expenses. The feedstock material in WAAM – the metal wire, is roughly ten percent of equivalent

weight of metal powder [4, 17], not only making it a cheaper option, but also an easier choice of feedstock to handle.

Further, WAAM machines can be readily adapted or modified from arc welding robots, making them more affordable than other M-AM instruments such as LPBF or LP-DED [4]. These synergic welding machines enable precise control over both the electric arc characteristics and wire movements, thereby expanding the capabilities to operate at lower energy levels and process a variety of material systems with regulated heat input (HI), superior weld quality, and reduced spatter during the deposition process [16, 25]. Metals that possess favorable weldability characteristics are expected to have the potential to be processed via WAAM [4]. In the past, researchers have successfully manufactured 3D parts using titanium-based [32, 33], aluminum-based [13, 34], steel-based [3, 4, 9, 15, 16, 35], and nickel-based alloys [36]. Stainless steels, including austenitic, martensitic, and duplex stainless steels, are suitable for WAAM because of their superior mechanical qualities and strong resistance to corrosion [8, 15, 37, 38].

1.2 COMPLEXITIES & CHALLENGES WITH WAAM

WAAM offer several benefits, particularly in terms of design freedom, and the ability to fabricate large-scale components in shorter lead times. However, these benefits are insignificant if the fabricated part is riddled with defects that might compromise its mechanical, physical, and/or chemical properties, making it unsuitable for use. Therefore, it is quintessential to ensure that the parts produced via WAAM technology are defect free and comparable to those fabricated via other M-AM techniques and/or traditional methods, in terms of part properties and performance. Process parameters, such as deposition paths and heat input, have shown to cause defects during deposition [4]. A complex deposition path can lead to issues such as spatter ejection or insufficient fusion, resulting in the formation of voids or gaps in the affected areas [39]. Parameters such as wire feeding speed, scanning speed, welding current mode, cooling time, and interlay temperature are known to play a significant role in determining the macroscopic characteristics [2, 4, 6, 13, 39]. Additional research to enhance the dimensional accuracy and surface quality of WAAM parts by optimizing these process parameters is required. The microstructures of WAAM stainless steel were also seen to be heavily influenced by the thermal history during the processes [40-42]. During the WAAM processing, the thermal history, which involves multiple cycles of heating and cooling, leads to the formation of non-equilibrium microstructures in the deposited parts [40]. **Table 1** (inspired from the study by Albannai et. al.) outlines the common defects and their possible causes [43].

Table1: Common defects and their possible causes outlined by Albannai et. al. [43] from past literature study

Type of Defect	Possible Causes	References
Pores	<ul style="list-style-type: none"> • Improper process parameters • Improper inter-pass layer temperature • Bad wire quality • Insufficient alloy composition • High cooling rate 	[44-49]

	<ul style="list-style-type: none"> • Presence of Hydrogen atmosphere 	
Lack of Fusion	<ul style="list-style-type: none"> • Low energy and heat input • Improper torch angle • Improper joint edge preparation • Inappropriate weld position • Insufficient filler wire material • Inappropriate weld speed • Unstable weld pool dynamics • Complex thermal cycle • Inappropriate weld set-up • High weld spatter • Insufficient flow of shielding gas 	[4, 50-52]
Cracks	<ul style="list-style-type: none"> • Alloy with high solidification range and/or un-weldable alloy • High thermal and/or mechanical stresses • High heat input • Large columnar grain formation • Large mushy zone size and/or large HAZ • Inappropriate weld pool motion and/or hydrogen gas around weld pool • Insufficient filler wire material 	[53-61]
Residual Stresses & Distortion	<ul style="list-style-type: none"> • Insufficient weld process parameters • Complex thermal cycle • Improper pre-heating temperature and/or heat input and/or inter-pass temperature • Inadequate deposition path 	[23, 62-68]

The most common defects observed in stainless steel parts produced by WAAM were found to be porosity (such as cracks, keyholes, lack of fusion, and gas porosity), undercutting, residual stresses, non-homogeneous microstructure, unbalanced chemical composition, nucleation of brittle phases, and anisotropic properties [69]. A few representative images of the defects in WAAM encountered by researchers in the past are compiled in **Figure 3**. Porosity is the presence of empty spaces or cavities within the weld bead, while undercutting is linked to the concavity of the weld bead, both of which can negatively impact the weld's performance. Lack of fusion (LOF) defects occur when particles from the material interact with the laser beam, while humping is characteristic to uneven material deposition.

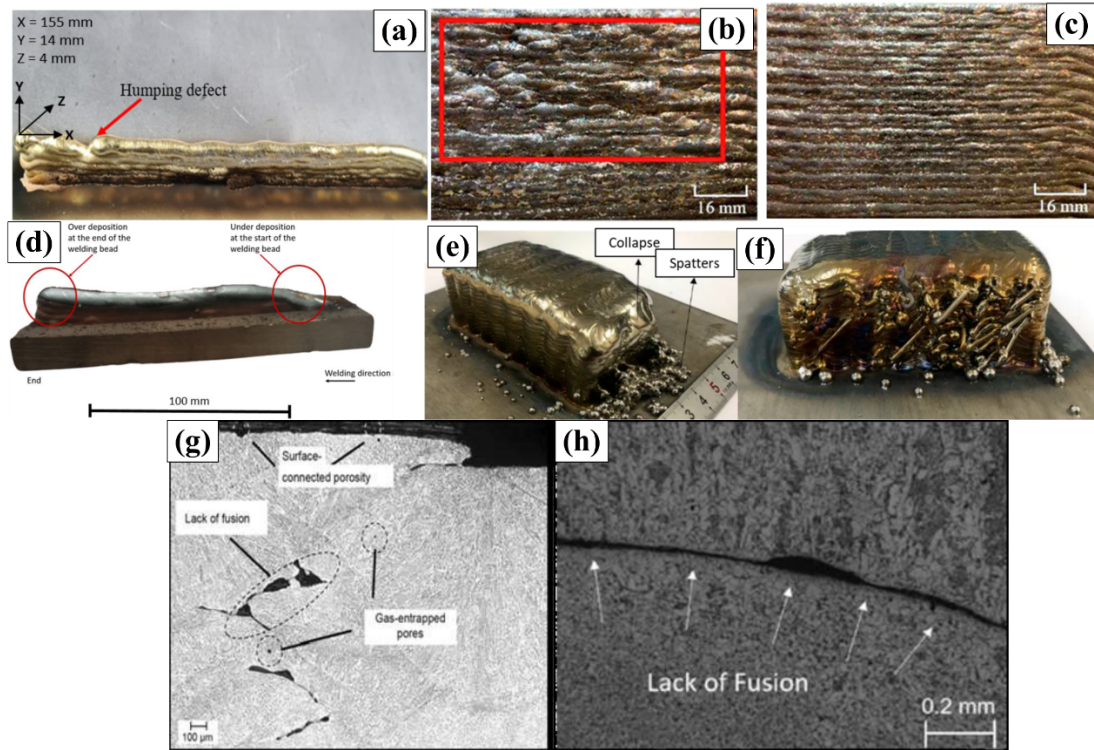


Figure 3: Common defects in WAAM observed by researchers in the past (a) humping defect in CuAl8 alloy [70] (b,c) surface features on walls fabricated with ER316LSi material at 10mm/s for 5s and 120s inter-pass time respectively [70, 71] (d) shape forming problems due to over and under deposition in welding [72] (e,f) macro-defects in WAAM showing spatter and un-melted wire respectively [12, 73] (g) Microscopic defects such as LoF and porosity in DED [43, 74] (h) LoF example in mild steel sample [43, 75]

Understanding the thermal history and residual stresses is critical in analyzing the distortion of WAAM parts especially as the volume of printed component increases, the impact of both factors becomes more prominent [76]. Geometrical dependencies and path planning strategies play a crucial role in understanding the thermal history of the part, where effective deposition path planning can greatly minimize residual stresses [77]. A few research studies primarily focused on welding paths with thin walls and simple shapes [78-81]. However, a deeper understanding of how variations in geometry affect the performance of thin and thick walls that further translate to larger components, is still lacking. Therefore, it is crucial to optimize and refine the WAAM deposition path, carefully manage the thermal history, and to study the impact of heat input, cooling rate, and reheating effect on the morphology, microstructure, and mechanical properties WAAM components.

2. PRECIPITATION HARDENED (PH) MARTENSITIC STAINLESS STEEL:

Precipitation hardened (PH) stainless steels were first introduced to meet the demand for high-strength, corrosion-resistant materials during World War II [38]. These materials are processable via common manufacturing techniques such as rolling, machining, forging, or welding, and can be strengthened through heat treatments post-fabrication [38]. On a broad level, PH steels can be

classified into three types based on the steel's response to cooling after being heated to temperatures beyond the austenizing temperature:

- i. Austenitic stainless steel
- ii. Semi-austenitic stainless steel
- iii. Martensitic stainless steel

17-4PH stainless steels (SS 17-4PH) is a type of martensitic precipitation hardened stainless steel that finds extensive applications in aerospace, defense, nuclear power plants, and oil & gas industries [9, 82]. SS 17-4PH is hardened primarily by martensitic transformation and copper precipitation in solution, where the most favorable properties in terms of strength, ductility, fatigue strength, and corrosion resistance are achieved through heat treatment. The nominal chemical composition of SS17-4PH and the yield strength, ultimate tensile strength, and % elongation at failure of 17-4PH post heat treatment (as mentioned by ASM handbook) are outlined in Table.

Table 2: Nominal composition of 17-4PH Stainless Steel and minimum mechanical properties required after heat treatment of 17-4PH, as outlined by ASM Handbook – Volumes 1 and 4

Nominal Composition %								
Cr	Mn	Si	Ni	P	S	C	Cu	Cb + Ta
15 – 17 %	1 % max	1 % max	3 – 5 %	0.04 % max	0.03 % max	0.07 % max	3 – 5 %	0.15 – 0.45 % max
Minimum Mechanical Properties								
Alloy – Heat Treatment (Reference)						Y.S (MPa)	UTS (MPa)	Elongation to failure
17-4 PH -H900 (ASM Handbook Volume 4)						1170	1310	10 %
17-4 PH -H900 (ASM Handbook Volume 1)						1055	1380	15 %

2.1 MARTENSITIC PHASE TRANSFORMATION IN 17-4PH STAINLESS STEEL

The well-known Fe-Fe₃C phase diagram is based on the assumption of very slow cooling rate at equilibrium conditions without any additional alloying elements, and therefore includes the identification of equilibrium phases such as austenite, pearlite, α -ferrite, δ -ferrite, and Fe₃C. The actual phase compositions in a given steel (ferritic, austenitic, martensitic, or duplex) is determined by the chemical composition of alloying elements, temperature, and cooling rates. Especially when utilizing different manufacturing techniques such as casting, welding, or additive manufacturing, cooling rates are much faster than those assumed for equilibrium conditions, thereby leading to the development of additional metastable phases which might not be identified in the equilibrium Fe-Fe₃C phase diagram [83].

Martensite is one such intermediate, metastable phase that occurs between the transformation from close packed face centered cubic parent austenite (γ) phase to a body centered cubic ferrite (α) crystal. At high cooling rates, carbon dissolved in FCC austenite cannot diffuse out, leading to a distorted body centered tetragonal (bct) structure, with one axis elongated, where the tetragonality is defined by the c/a ratio of the unit cell [84]. Honda and Nishiyama developed a linear

relationship between the tetragonality of the martensite and the carbon content, for steels with carbon content greater than 0.6% [85].

$$c/a = 1 + 0.045 * (\text{wt.\% C})$$

However, because of the extremely low amounts of carbon in SS 17-4PH, the c/a ratio of the crystal is nearly 1. The intermediate behavior of a unit cell of the parent FCC austenite rotated at 45° angle resulting in the unit cell of BCT martensite is known as Bain correspondence of martensite [86]. Further, the crystallographic orientation between the parent austenite and low carbon martensite is described by Kurdjumov-Sachs (KS) relationship [84, 87, 88].

Martensite formed can be of two different morphologies – lath and plate, based in the chemical composition and temperature. Lath martensite is often found in hypo-eutectoid steels whereas plate martensite (which is twinned), is the primary formed in hyper eutectoid steel alloys with medium carbon and higher nickel content [83]. However, some previous studies showed evidence of martensitic twinning in 17-4PH [87], but other studies report an absence of twinning [88].

Martensite phase formation proceeds upon cooling below a temperature, referred to as the martensite start temperature (M_s), whereas the temperature at which the complete microstructure of the material becomes martensite is known as the "martensite finish temperature" (M_F) [83, 84]. However, depending on the carbon content in the alloy, some amount of retained austenite exists in the microstructure despite reaching M_F temperature, due to high lattice stress caused by the lattice structure distortion during the martensite formation, preventing further nucleation of the martensite grains [83]. Based on the chemical composition, the approximate M_s of steel can be computed by the equation below [83].

$$M_s[^\circ\text{C}] = 539 - 423 \cdot \text{C}\% - 7.5 \cdot \text{Si}\% - 30.4 \cdot \text{Mn}\% - 12.1 \cdot \text{Cr}\% - 17.7 \cdot \text{Ni}\% - 7.5 \cdot \text{Mo}\% - 10 \cdot \text{Co}\%$$

M_s calculations were developed through experimental dilatometry measurements and are empirical in nature. Estimation of M_s helps understand the stability of austenite in final microstructure [84]. However, these equations do not include the effect of cooling rates, and this effect is better understood using time-temperature transformation (TTT) or continuous cooling transformation (CCT) diagrams. TTT and CCT diagrams are both used to understand the behavior of materials during cooling from a high temperature. TTT diagrams (**Figure 4**) predict the microstructure transformations of a material while cooling at different rates from a temperature above the austenite transus temperature (A_3) to the final temperature and held for a long period of time. CCT diagrams (**Figure 5**) on the other hand, show the transformation at different temperatures while continuously cooling at a given cooling rate.

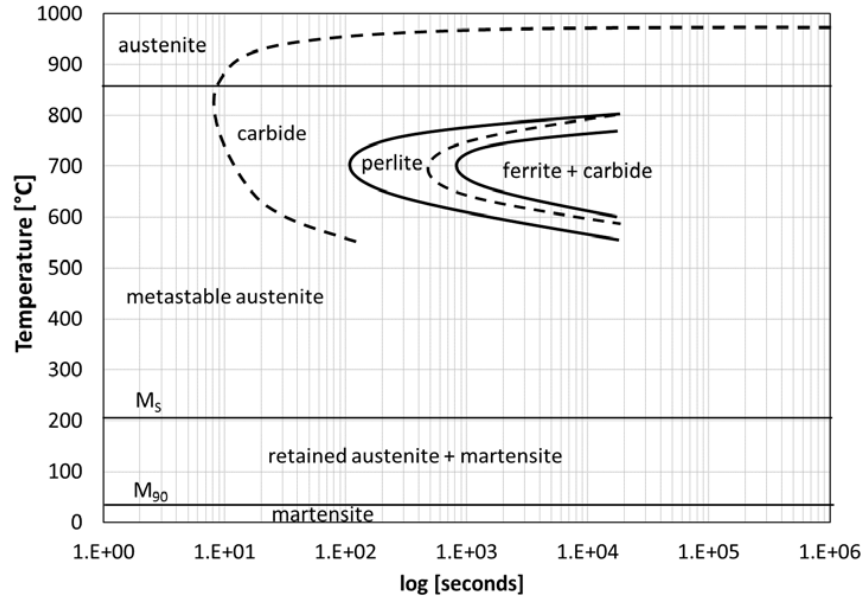


Figure 4. TTT Diagram of X39Cr13 stainless steel (comparable to AISI 420C) [83].

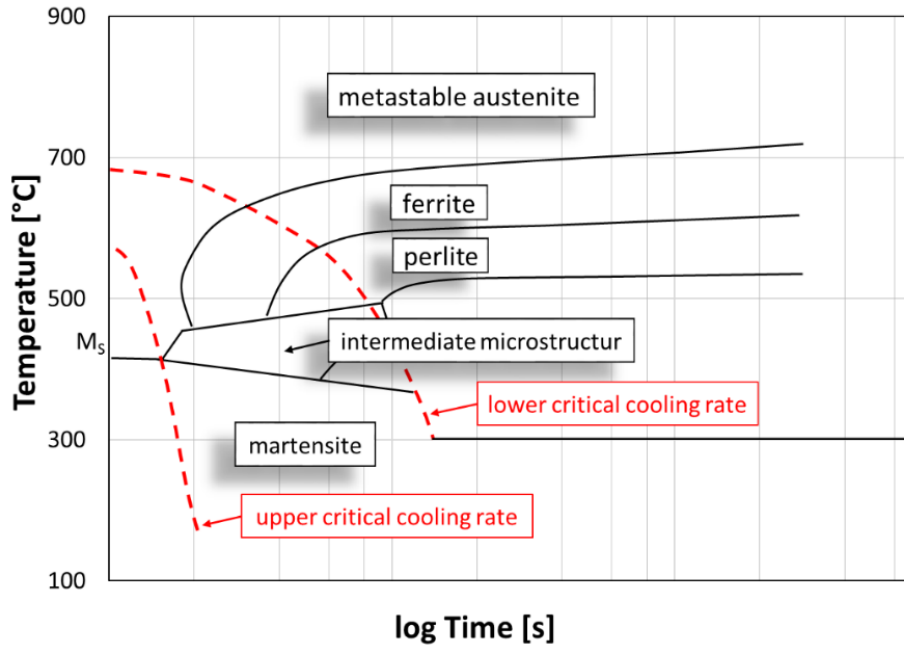


Figure 5. Continuous Cooling Transformation (CCT) diagram [83].

Furthermore, based on the alloying elements in precipitation hardened Cr-Ni stainless steels, these materials solidify in either primary ferritic or primary austenitic phases [83]. A ratio of chromium-equivalent and nickel-equivalent (Cr_{Equ} / Ni_{Equ}) is calculated based on the chemical composition of the alloy, which helps predict the primary solidification phase as shown in the **Figure 6** where δ -ferrite decreases with a decreasing Cr_{Equ} / Ni_{Equ} ratio during solidification of a Cr-Ni stainless steel with 72 wt.% Fe [83]. More information on calculating Cr_{Equ} , Ni_{Equ} , and predicting non-equilibrium phase formation in PH stainless steels is provided in the next section.

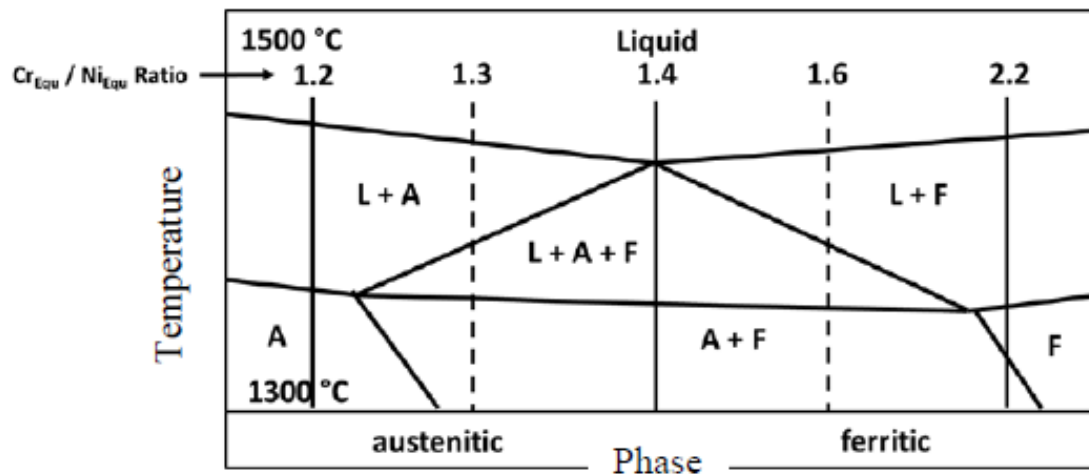


Figure 6: Illustration of a three-phase solidification diagram to determine the primary solidification phases on Cr-Ni stainless steels based on the ratio of Cr_{Equ} / Ni_{Equ} , where L is liquid, F is ferrite, and A is austenite phase [83, 89]

2.2 PREDICTIVE PHASE DIAGRAMS IN PH STEELS

Predictive phase diagrams were designed for stainless steels to forecast the microstructural changes resulting from welding these materials. The most renowned diagram among these is the Schaeffler diagram [90], which predicts phases based on the chemical composition of the alloy at ambient temperature. The initial diagram was created for a restricted range of compositions [90], while subsequent research led to modification in chromium and nickel equivalent models for different alloys. **Table 3** provides several chromium and nickel equivalents.

Table3: Evolution of calculations for equivalent chromium and equivalent nickel concentrations from 1949 to 2000's [84]

Cr _{Eq}	Ni _{Eq}	Source
Cr + Mo + 1.5Si + 0.5Nb	Ni + 30C + 0.5Mn	Schaeffler (1949)
Cr + 2Si + 5V + 5.5Al + 1.75Nb + 1.5Ti + 0.75W	Ni + Co + 0.5Mn + 0.3Cu + 25N + 30C	Pickering (1984)
Cr + Mo + 1.5Si + 0.5Nb	Ni + 0.5Mn + 30C + 30N	Delong (1960)
Cr + Mo + 0.7Nb	Ni + 35C + 20N + 0.25Cu	WRC-1992 Koteki <i>et al.</i> (1992)
Cr + 1.21Mo + 0.48Si + 0.14Nb + 2.27V + 0.72W + 2.20Ti + 0.21Ta + 2.48Al	Ni + (0.11Mn - 0.0086Mn ²) + 24.5C + 14.2N + 0.41Co + 0.44Cu	Hull (1974)
Cr + 2Mo 10(Al + Ti)	Ni + 35C + 20N	Balmforth & Lippold (2000)

Predominantly, two diagrams are used to predict the resultant material microstructure in welding applications, where rapid cooling is experienced. The Schaeffler diagram (**Figure 7**) illustrates the

phase fields and iso-ferrite lines, to predict the primary microstructure of a weld and estimate the δ -ferrite content, based on the chemical composition of the stainless-steel alloy [83, 90]. It is not a precise phase diagram, but rather an estimation that aids in predicting the microstructure of stainless steel weldments at room temperature, after being cooled from higher temperatures [83]. It is a useful tool for determining the presence of ferritic, martensitic, and austenitic phases in corrosion-resistant steels with a carbon content of up to 0.25 mass %, based on the values of Cr_{Equ} and Ni_{Equ} [83].

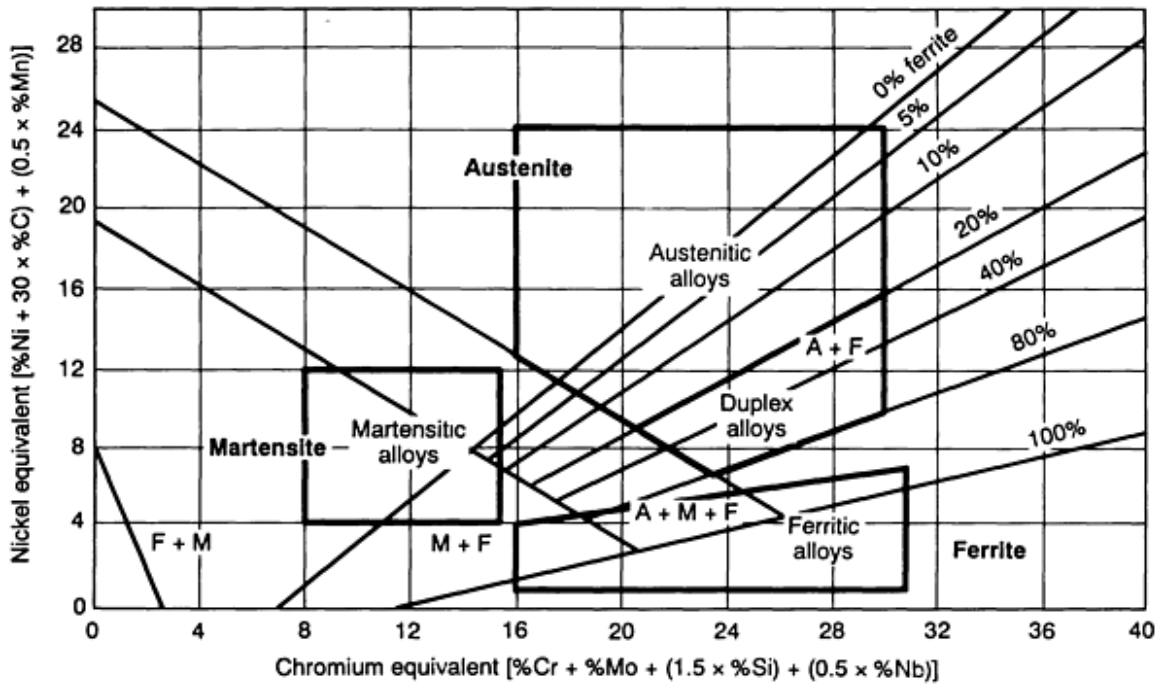


Figure 7: Original Schaeffler Diagram [84, 90]

Initially, the Ni_{Equ} value utilized in the Schaeffler Diagram did not account for the nitrogen content that creeps in during gas atomization for powder production, and while maintaining an inert atmosphere in manufacturing processes like LPBF [83]. In the 1970s, DeLong made revisions to the diagram and equation for $Ni_{Equ-mod}$ in order to accommodate the addition of nitrogen content (N%) [91]. Later in 1992, Koteki et. al took into account, the influence of Cu, and the $Ni_{Equ-modCu}$ was further modified as shown in equations below and incorporated these values to predict microstructural phases as shown in **Figure 8** [92, 93]

$$Ni_{Equ-mod} = Ni\% + 0.5 Mn\% + 30 C\% + 30 N\%$$

$$Ni_{Equ-modCu} = Ni\% + 0.5 Mn\% + 30 C\% + 30 N\% + 0.25 Cu\%$$

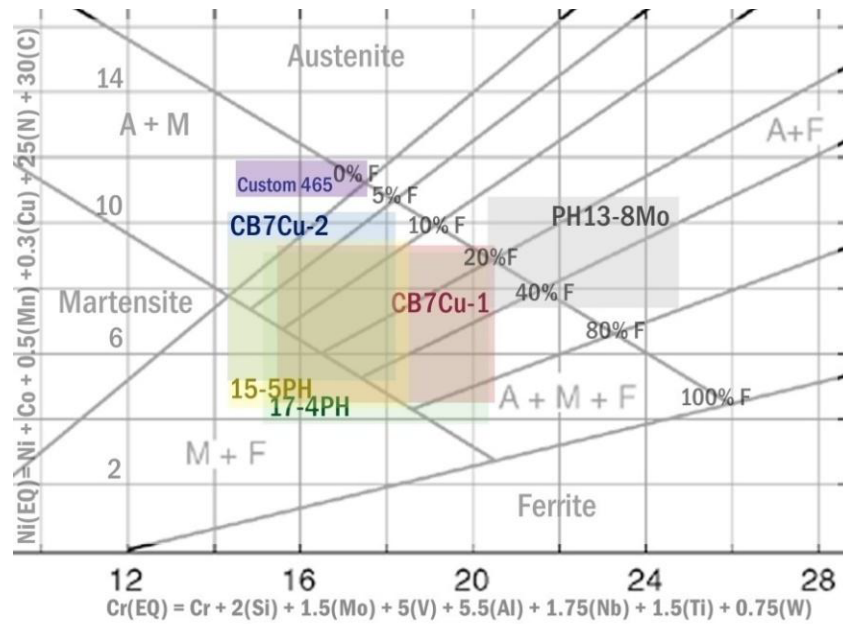


Figure 8: High Strength Precipitation Hardened Steels on Modified Schaeffler Diagram [84]

The Delong diagram depicted in **Figure 9** is an additional phase prediction tool that demonstrates that when the nitrogen percentage in S17-4 increases, the δ -ferrite percentage declines [83]. However, the usefulness of these diagrams to predict relative amounts of austenite, martensite and ferrite is limited, as they only state the estimated boundaries of where martensite may begin to form or where a material may become fully martensitic, while some studies completely exclude austenite formation and focus only on martensite + ferrite boundaries [84, 94].

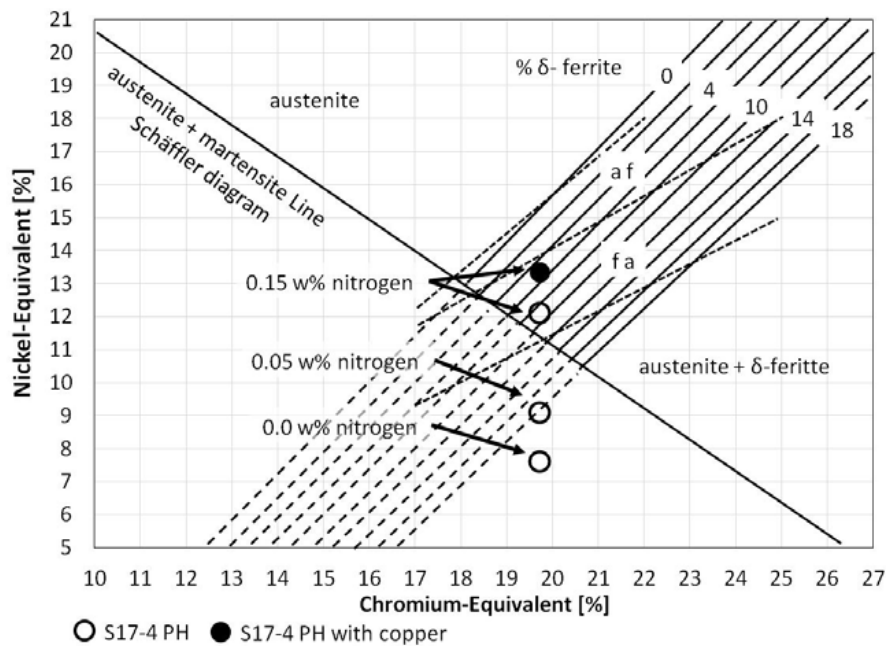


Figure 9: Possible microstructure of S17-4 according to the Delong Diagram [83].

2.3 HEAT TREATMENT FOR STRENGTHENING 17-4PH STAINLESS STEEL

SS 17-4 pH being a precipitation hardened steel, undergoes two stages of heat treatment: solution treatment and ageing. In solution treatment (ST) it is subjected to high temperature to solubilize the alloy element present and to avoid grain growth. Although ST results in martensitic structure, it lacks high hardness [9]. Aging treatment on the other hand promotes strength due to Cu-rich precipitates but can reduce the toughness of the material [9]. A significant portion of the strengthening in precipitation hardened steel is attributed to the post-quench aging process. The age hardening process has two main objectives: a) to strengthen the low-carbon martensite, enhancing its toughness, and b) to facilitate the production of copper-rich precipitates [84]. The SS 17-4PH alloy, regardless of whether it is in the form of wrought or cast, undergoes an aging process at temperatures ranging from 900 to 1150°F for different durations [84]. **Table 4** outlines the aging guidelines and minimum properties of cast and wrought 17-4PH stainless steel heat treated under different conditions, as described in ASTM A554/A564M and ASTM A747 standards.

Table 4 - Aging Guidelines and Minimum Properties, 17-4PH Cast and Wrought [84]

Condition	Age Temp (F°)	Age Time (h)	Cooling	YS/TS min CAST (ksi)	YS/TS min WROUGHT (ksi)	% Elongation [CAST]/ [WROUGHT]
H900	900	1.5	Air Cool	145/170	170/190	5/10
H925	925	1.5	Air Cool	150/175	170/155	5/10
H1025	1025	4	Air Cool	140/150	155/145	9/12
H1075	1075	4	Air Cool	115/145	145/125	9/13
H1100	1100	4	Air Cool	110/135	140/115	9/14
H1150	1150	4	Air Cool	95/125	135/105	10/16
H1150M	1400 1150	2 4	Air Cool	-	-	-
H1150DBL	1150 1150	4 4	Air Cool	-	-	-

SS 17-4PH undergoes aging for durations ranging from 1.5 to 4 hours at temperatures of 900°F, resulting in the formation of copper-rich precipitates [84]. Slightly overaged precipitates, typically in the form of very fine fcc-precipitates, have been seen in majority of the studies [87, 95-97]. (**Table 5**). Murayama et. al. observed, very fine, homogenous copper rich precipitates 150Å in size after 2 hours of aging at 510°C (950°F) [98], while Wu and Lin [99] observed short ellipsoid-like precipitates after aging at 600°C. Despite some studies not being able to identify the precipitate under peak-aging conditions [87, 88, 99, 100], there was a clear increase in strength at peak age conditions which was hypothesized to be due to the coarsening of precipitates at higher temperature and time of H1100 treatment. Past literature also indicates that the apparent increase in strength at a certain age is primarily due to modulus hardening [88]. This was thought to be produced by a discrepancy in elastic moduli between the precipitate and the matrix [84]. Observing precipitates has been challenging in many instances, even with the use of TEM, mostly due to the small size of the precipitates and the high dislocation density of the lath structure found in low carbon martensite [84].

Table 5 - Precipitate found in past work on 17-4 PH stainless steels [84]

Study	Heat Treatment Conditions	Precipitate	Detection Method
Rack and Kalish (1974)	510°C / 2hr 600°C / 2 hr	Cu-rich precipitate (fcc) Cu (fcc) precipitate	TEM TEM + SAD
Murayama (1999)	510°C / 2hr 400°C / 5000h	Incoherent 50% at weight Cu precipitate (bcc) Large Cu (fcc) precipitate + ultrafine Cu-rich precipitate	FIM- Atom Probe + TEM
Hsiao et. al (2001)	480°C / 1 hr	15nm x 25nm Possible fcc precipitate, not well identified	FEG-TEM
Wu and Lin (2003)	600°C / 0.25-32hr	Incoherent Cu fcc precipitate	TEM
Viswanathan (1988)	510°C / 2 hr	150 Å (fcc) precipitate	TEM + SAD

2.4 WELDING 17-4PH STAINLESS STEEL: PAST LITERATURE

17-4PH martensitic stainless steel has shown tremendous results in weldability and strengthening via post-weld heat treatments (PWHT) from as early as 1960's [37, 38]. It offers the opportunity to customize mechanical properties of the component through precisely programmed heat treatments. The material achieves high strength through the formation of small, dispersed Cu-rich phases within the martensitic matrix during the ageing process [101]. The changes that occur in the fusion zone of a weld can resemble those seen in WAAM depositions [9]. However, most of the research conducted on the weldability of 17-4 pH steel concentrates on examining how the microstructure and mechanical properties differ from the base material. There have been limited studies on how the weld microstructure affects the properties of the weld [102, 103]. Rather, much of the focus in welded 17-4PH has been on understanding the changes in microstructure and hardness in the heat affected zone (HAZ) [37, 102-104].

In 1989, Bhaduri et. al. [104] conducted a thorough investigation into the microstructure and hardness of the heat-affected zone (HAZ) under various weld heat inputs and starting conditions. It was observed that, irrespective of the heat input applied during the welding of 17-4 PH in condition A and H900, there was a noticeable decrease in hardness compared to the base metal. This was attributed to reformed austenite in HAZ and solutionization of existing precipitates. Additionally, factors such as ageing and tempering of martensitic structure were stated to be contributing towards softening of the HAZ. Later in 1995, Bhaduri et. al [37] conducted experiments to analyze the impact of different heat treatment combinations, including aging the material in its original welded state, both with and without a prior solution treatment. It was found that in order to use 17-4 PH in the H900 condition for practical purposes, it is necessary to perform a preliminary solution treatment (ST) before aging to ensure desirable properties. It was also

discovered that the preliminary ST before the aging can decrease the variations in hardness, leading to a more homogenous microstructure [105, 106].

However, almost all the studies primarily examined single pass welding and the potential changes in the microstructure with an increased number of passes (layers), or the possibility of achieving similar results in multi pass welding scenarios were not considered. One study by Hamlin et. al. in 2017 [107] discussed multi pass welding of 17-4 PH. However, this work only explored the impact of two welding passes along the base plate at three different heat inputs (1000, 2000, and 3000J/mm), on microstructure and hardness as shown in **Figure 10**. This however, is not sufficient to gain valuable understanding of WAAM deposition of 17-4 PH. The process of cooling and reheating between multiple layer can cause negative impacts on the microstructure of a multi-pass welded 17-4 PH part. Therefore, it is important to consider the impact of repeated heating and its cumulative effects, particularly when attempting to apply this knowledge to a process like WAAM.

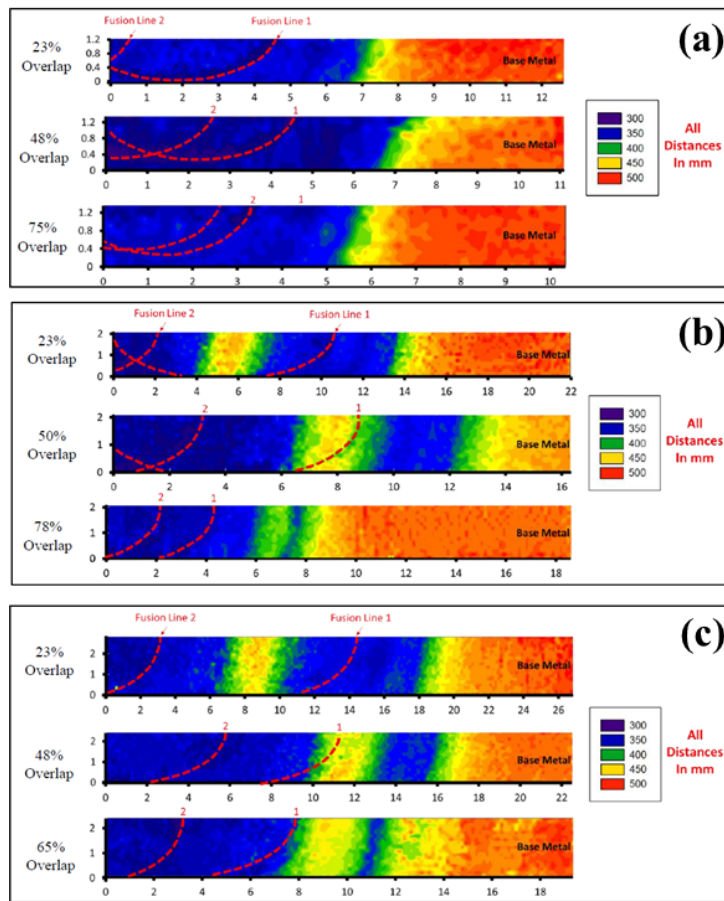


Figure 10: Hardness maps measured across a dual-pass weld of 17-4PH with 25%, 50%, and 75% target overlaps made at (a) 1000 J/mm heat input (b) 2000 J/mm heat input (c) 3000 J/mm heat input [107]

Despite the extensive efforts, the research conducted on welding and the impact of PWHT on microstructure and mechanical properties of 17-4PH components is limited to a few welding passes and does not accurately reflect the thermal conditions involved in WAAM. According to a study by Zhao et al. [108] on WAAM of T-6Al-4V, the last few layers of deposited material in

WAAM exhibit a distinctly different microstructure compared to earlier layers. This difference of the part, and was to be attributed to the incomplete thermal cycles experienced by this particular section and was expected to be as large as 10-12mm based on their findings. Such differences in microstructure and ensuing part properties can be expected in WAAM of 17-4PH as well, and it is crucial to understand these differences.

2.5 WIRE ARC ADDITIVE MANUFACTURING (WAAM) OF 17-4PH STAINLESS STEEL

SS 17-4PH finds applications in aerospace, energy, and food processing due to its excellent chemical and mechanical properties, and has also gained significant interest in the additive manufacturing community because of its exceptional weldability [109]. Prior studies on the additive manufacturing of 17-4 PH stainless steel have primarily focused on laser+ powder processing. This involves the creation of 3D components by melting a metallic powder bed layer by layer using a laser beam. Several studies have concentrated on examining the microstructure and mechanical characteristics of selective laser melting (SLM) of 17-4 PH stainless steel [3]. One notable feature of laser-based additive manufacturing (AM) processes is the rapid heating and cooling rates during fabrication, which leads to a more refined microstructure when compared to conventionally manufactured (CM) counterparts [109]. The structure of the material, including features like grain structure, texture, surface roughness, and defect structure, plays a big role in determining its mechanical performance, which in turn is influenced by the thermal history of the material during manufacturing [109].

Given the similarities between fusion welding and metal additive manufacturing, it is interesting to investigate the current state of this field in relation to 17-4 PH, particularly arc-based welding techniques, which share principles with WAAM. However, currently available literature on WAAM of 17-4PH is very limited [3, 9, 109]. The study conducted by Martina et al. in 2018 [9], was the first to explore WAAM deposition of 17-4 PH. However, the primary focus of this work was on determining the potential for achieving high deposition rates in the manufacturing process via WAAM and not on the material system itself. In this study, various deposition techniques using the WAAM tandem torch process (**Figure 11**) were explored, with the goal to achieve a high deposition rate of 17-4PH stainless steel. The contact tip to work distance, gas flow rate, layer height, torch angle, and gas flow pressure were kept constant, while the wire feed speed (WFS) and travel speed (TS) were varied within a range of 7.5–10.5 m/min and 1–1.5 m/min. respectively in a shielding gas atmosphere of 2.5% CO₂ in Argon [9]. Optical microscopy and hardness testing was on vertical and horizontal cross sections. However, not enough information was provided about the microstructure, mechanical properties, or post-manufacturing heat treatments required to achieve desirable properties.

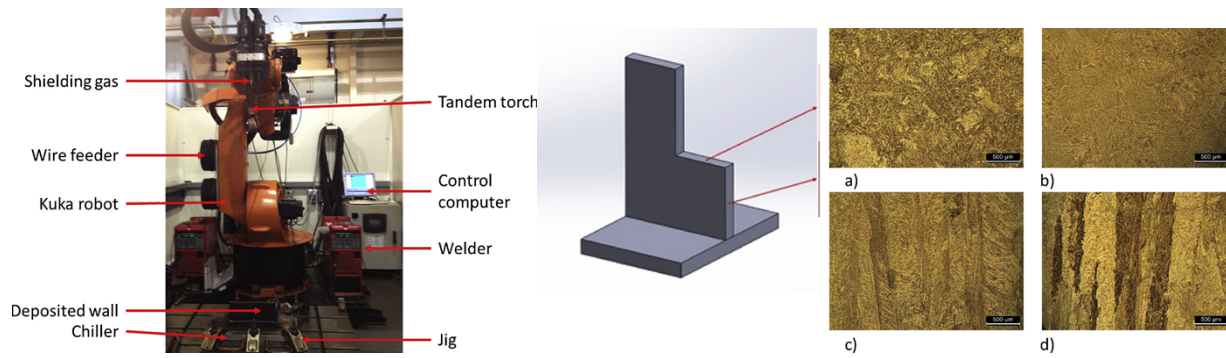


Figure 11: (a) Pulse MIG welding tandem torch experimental setup. (b) Microstructure comparison, a) Horizontal phase at WFS 7 m/min; b) Horizontal phase at WFS 8 m/min; c) Vertical phase at WFS 7 m/min; d) Vertical phase at WFS 8 m/min [9].

A study conducted by Caballero et al. [3] in 2019, examined the microstructures of CMT 17-4 PH stainless steel samples under four different heat treatment conditions. These conditions included as-deposited (AD), as-deposited plus H900 (480°C, 1h) ageing treatment (AD + H900), and as-deposited followed by solution treatment (1040°C, 0.5h) and H900 ageing (ST + H900). The results of this research are shown in **Figure 12**. The composition of the shielding gas (SG1) used was 38% He and 2% CO₂ + Ar. The Cr_{eq}/Ni_{eq} ratio of 17-4 PH stainless steel feedstock used in this study exceeds 1.55, resulting in a primary ferrite solidification mode. During the cooling process, the alloy 17-4 PH undergoes a phase transformation sequence. It starts as a liquid (L), then transforms into δ-ferrite, followed by the formation of γ-austenite followed by δ-ferrite before finally transforming into a combination of martensite and δ-ferrite [103]. However, the rapid cooling rates experienced during WAAM processing limit the transformation of δ-ferrite to γ-austenite, causing some δ-ferrite to remain at room temperature [3]. This is evident from the microstructure of dendritic martensite-δ ferrite in the as-deposited condition sample (**Figure 12a**). In addition, a significant portion of the δ-ferrite undergoes a transformation into austenite, which then further transforms into martensite as a result of the relatively slower cooling rate when temperatures exceed the A3 point. Consequently, the microstructure primarily consists of martensite, in samples heat treated under ST+H900 condition as depicted in **Figure 12c** [3].

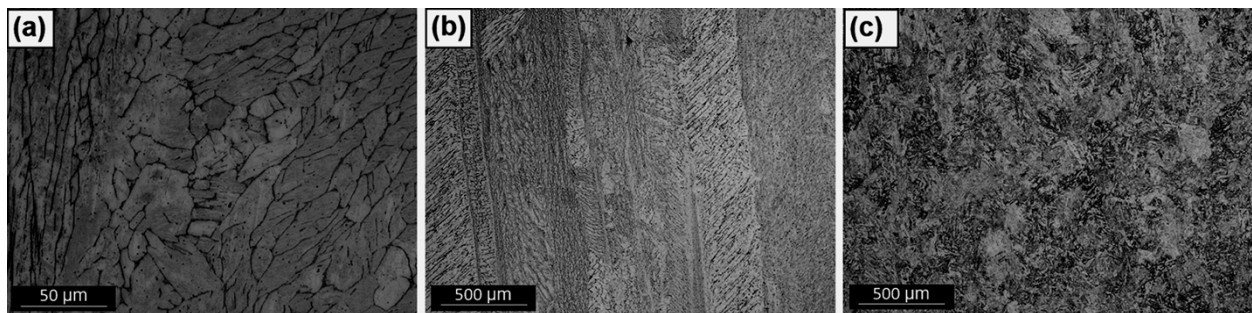


Figure 12: Microstructure: (a) As-deposited condition of sample manufactured with SG1; (b) Sample used for tensile testing, AD+H900 condition; (c) Sample used for tensile testing, ST+H900 condition [3]

Further, this study [3] also examines the impact of the composition of the shielding gas (SG) on the resulting microstructure, in addition to studying the effect of different deposition strategies on

part properties. Three different deposition strategies were studied: single pass deposition, oscillated and parallel pass (**Figure 13**). In a single pass deposition strategy, each layer is formed by a single bead of deposited molten metal, whereas in the oscillated path, the torch moves with a specific oscillation width to form wider layers [3]. Parallel pass deposition strategy on the other hand consisted of a sequence of single beads deposited next to each other [3]. These differences in deposition strategies were expected to induce different thermal cycles in the deposited metal due to dissimilar thermal masses and heat accumulation, leading to differences in part properties in as-deposited (AD) and heat-treated conditions [3]. It was discovered that using SG1 (Shielding gas 1: 38% He + 2% CO₂ + Ar) resulted in a lower percentage of retained austenite, in contrast to using SG2 (Shielding gas 2: 2.5% CO₂+Ar). This was attributed to the presence of He in SG1, causing a higher heat input (HI) and resulting in a lower cooling rate when using SG1 [110]. It was suggested that the higher HI in SG1 assisted grain growth thereby leading to larger grains in samples fabricated with SG1 as opposed to finer grains in samples fabricated with SG2. These smaller grains signify increased yield strength, leading to a decrease in martensite start temperature. In other words, smaller grains inhibit complete transformation of retained austenite to martensite, leading to higher percentages of retained austenite in the microstructure [111].

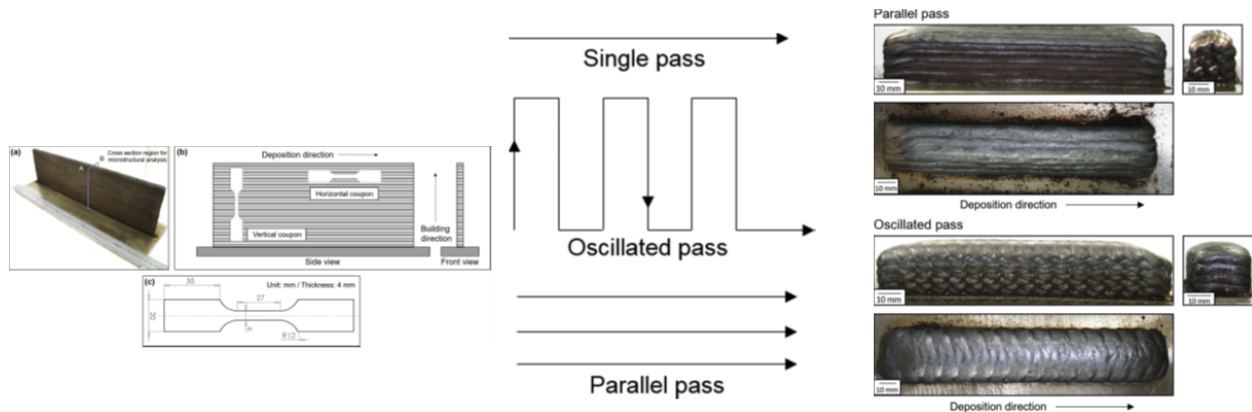


Figure 13: (a) Sample extraction strategy to obtain horizontal and vertical coupons for tensile testing (b) Different deposition strategies used in the work by Caballero et. al. (c) Top view and side view of samples deposited using different deposition strategies [3].

An increase in hardness was observed in samples aged directly from as-deposited (AD) condition without any solution treatment (ST) due to the precipitation of coherent Cu-rich precipitates in martensite during ageing, as shown in **Figure 14** [105]. Additionally, it was shown by [112] that δ -ferrite can also experience an increase in hardness because of the nucleation and growth of precipitates, which explained why in some cases, hardness values for the AD+ H900 samples are higher than the ones obtained for ST+H900. Solution treated samples were also seen to be softer and had a homogenous microstructure due to the dissolution of precipitates back into the solid solution during ST [3]. Further, there was no noticeable trend in hardness with different deposition strategies. This fluctuating behavior in hardness with different deposition strategies was attributed to the variations in the amount and size of Cu-enriched precipitates in builds experiencing different thermal cycles. A study by Xiong et. al. from 2017 [113] suggests that every time a new layer is deposited, the temperature can repetitively increase up to at least 450°C. Such repetitive thermal cycles inherent to the WAAM process define the microstructure and ensuing part properties.

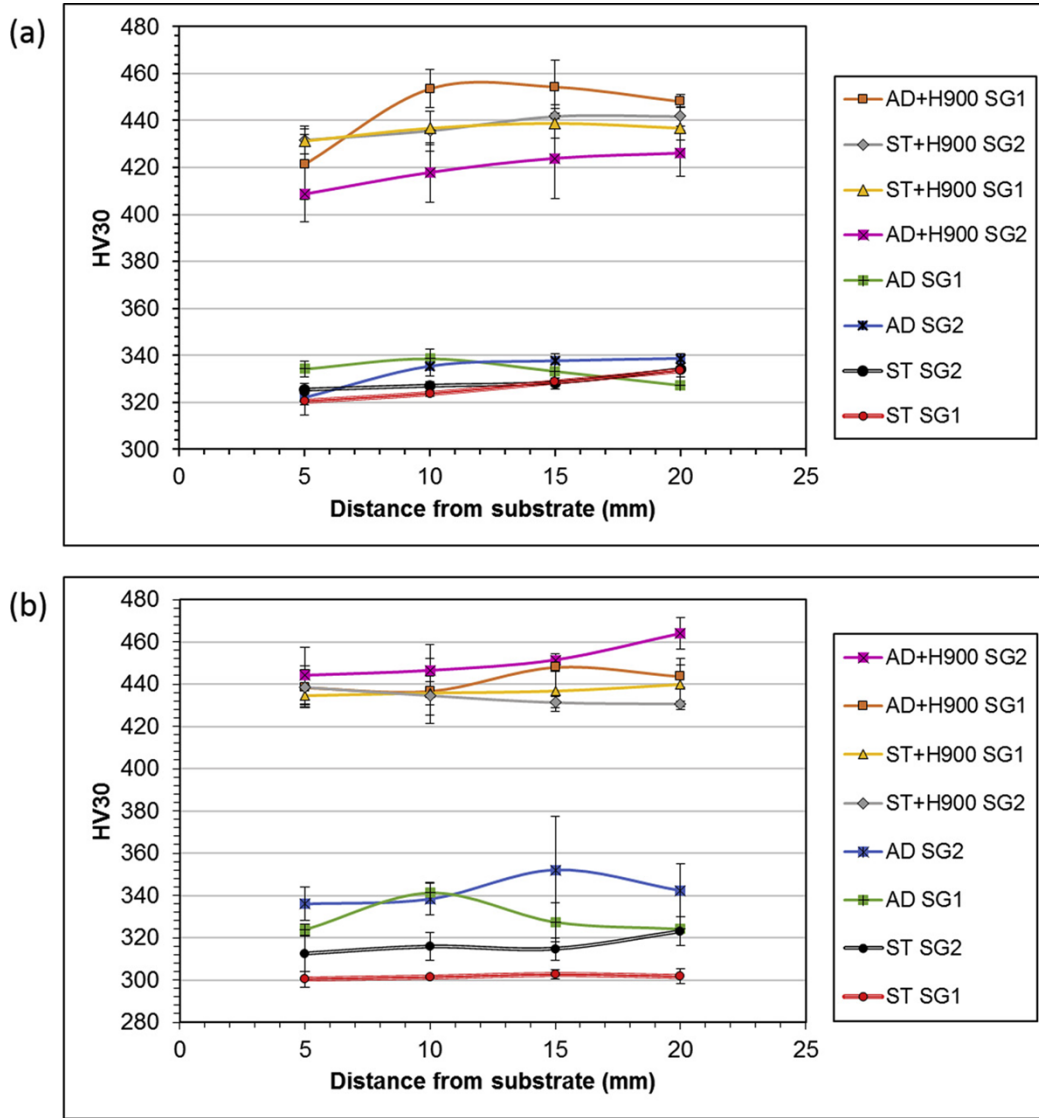


Figure 14: Vickers hardness measurements of as-deposited, and heat treated 17-4PH stainless steel fabricated via WAAM by Caballero et. al. under different scan strategies [3].

Tensile test results were used to understand the influence of different phases (lath martensite and δ -ferrite) on mechanical properties (**Table 6**). Solutionizing heat treatment prior to ageing was seen to be necessary to achieve desired properties, as this condition guarantees a homogenous microstructure of nearly 100% lath martensite where segregated elements and precipitates have dissolved back into solid solution during ST. Fractography of the sample in ST+H900 condition showed a fracture dominated by multiple equiaxed dimples corresponding to ductile behavior (13.8% elongation) as shown in **Figure 15**. A network of smaller dimples was seen, which were hypothesized to be related to the voids initiating in very fine second phase particles generated during the ageing step [114].

Table 6: Tensile property results for different thermal processing conditions of WAAM 17-4PH parts printed by Caballero et. al. [3], where AD = as-deposited, ST – solution treated, H900 is tempering heat treatment condition.

Condition	Sample Direction	Yield Strength (MPa)	UTS (MPa)	% Elongation
AD	Vertical	738 ± 30	979 ± 13	12.2 ± 0.7
	Horizontal	842 ± 65	1009 ± 55	11.6 ± 0.3
AD + ST	Vertical	827 ± 4	1006 ± 6	12.4 ± 0.4
	Horizontal	815 ± 24	1000 ± 5	12.8 ± 0.2
AD + H900	Vertical	1059 ± 9	1124 ± 5	6.5 ± 0.3
	Horizontal	1140 ± 57	1293 ± 32	8.2 ± 1.3
ST + H900	Vertical	1234 ± 33	1351 ± 11	13.8 ± 0.5
	Horizontal	1225 ± 36	1353 ± 6	13.8 ± 1.4

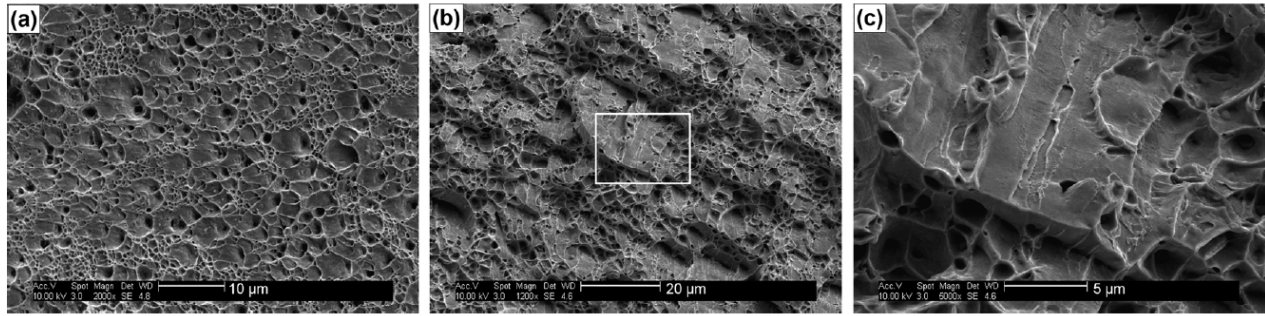


Figure 15: Fractography of spent tensile specimen in (a) ST + H900 (b) AD + H900 (c) AD + H900 (higher magnification) conditions [3].

In 2022, Nezhadfar et. al. [109] explored the differences in laser powder bed additively manufactured (LPBF) and laser powder direct energy deposited (LP-DED) 17-4PH stainless steel, in terms of microstructural characteristics and mechanical properties. Non-heat-treated (NHT) microstructures of LPBF and LP-DED 17-4PH SS specimen microstructures were characterized using EBSD and ECCI. L-PBF samples were seen to have fine, equiaxed, ferrite grains, as compared to the coarse columnar ferrite grains in LP-DED samples. The ECCI images also revealed ferrite and lath martensite microstructure in LPBF samples, whereas the LP-DED specimen had a ferritic microstructure consisting of massive ferrite grains with Widmanstatten ferrites decorating the grain boundaries (**Figure 16**). Since the martensite start temperature ($M_s = 100\text{--}150^\circ\text{C}$), is above room temperature for the 17–4 PH SS [115, 116] the austenite formed during solidification transforms to the martensite upon cooling to room temperature. However, the ferritic microstructure in as-printed NHT samples was attributed to the “austenite by-passing” mechanism, where the ferrite phase formed from the liquid will not transfer to the austenite due to the high cooling rate in AM processes as compared to conventional manufacturing techniques [117]. The presence of lath martensite in LPBF samples and not in LP-DED samples was attributed to the faster cooling rates of LPBF (2-3 orders of magnitude higher compared to LP-DED) and the higher C_{eq}/Ni_{eq} ratio of LP-DED 17-4PH (~ 2.9) compared to LPBF powders (~ 2.1) used in this study.

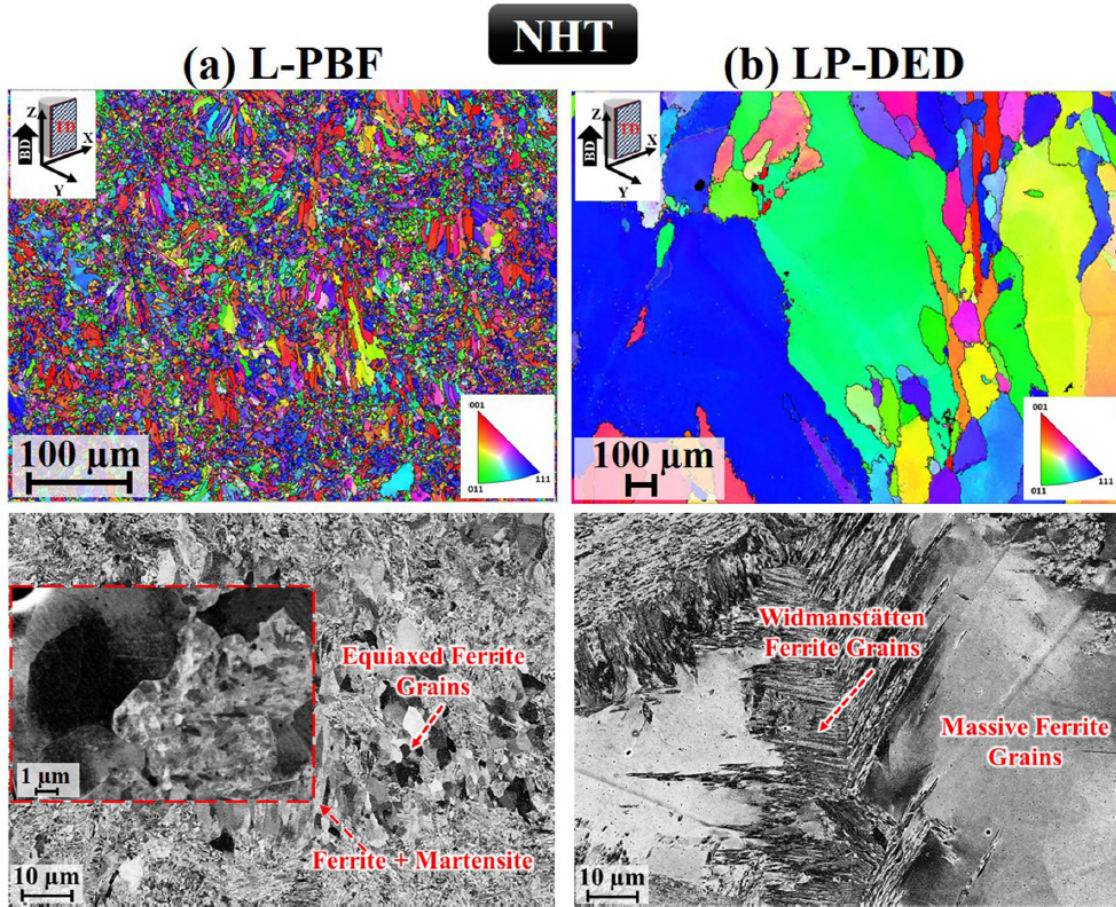


Figure 16: Inverse pole figure (IPF) maps along the Z direction and ECCI micrographs of (a) L-PBF, and (b) LP-DED 17-4 PH SS specimens in NHT condition [109].

An interesting aspect of this research was the examination of the effect of post-printed heat treatments on the microstructure and mechanical properties. NHT LPBF and LP-DED samples were each subjected to CA-H900 and CA-H1150 heat treatments. It was seen that L-PBF and LP-DED samples subjected to CA-900 have a primarily martensitic microstructure with a minimal fraction of retained austenite ($\sim 0.1\%$), whereas after CA-1150 the fraction of retained austenite is increased for both the L-PBF and LPDED specimen (as shown in **Figure 17**). This increase in retained austenite in CA-1150 condition was explained by the diffusion of austenite stabilizers (Cu, Ni, N, etc.) to the grain boundaries during the long-term aging (4 h) at a temperature close to the austenite reversion, resulting in the nucleation of austenite grains [118]. Past literature also established that martensitic transformations are more difficult for finer austenite grains, which may be retained after heat treatment [119], which explains the higher percentage of retained austenite in LPBF-CA-H1150 samples compared to their LP-DED counterparts.

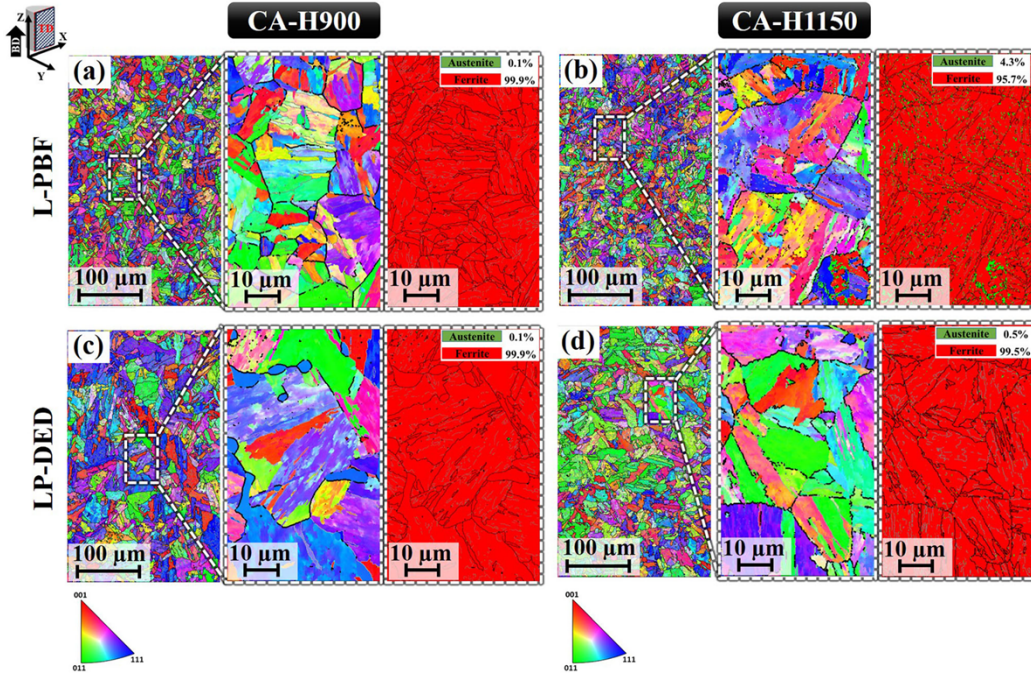


Figure 17: IPF maps (along the Z direction) and phase maps for the heat treated 17-4 PH SS specimens: (a) L-PBF and (c) LP-DED at CA-H900, and (b) L-PBF and (d) LP-DED at CA-H1150. Note that the black boundaries in the magnified IPF maps (in the middle) represent the prior austenite grain boundaries [109].

Mechanical strength of the specimens revealed that those fabricated via LPBF exhibited superior tensile strength and ductility compared to LP-DED specimens. Additionally, it was observed that peak-age (CA-H900) heat treatment resulted in the highest tensile strength at the expense of the ductility, whereas the over-aging (CA-H1150) reduced the strength and increased the ductility (**Figure 18**). This is due to the formation of nano-sized Cu-enriched precipitates after CA-H900 condition which coarsen upon over-aging, thereby resulting in higher ductility after CA-H1150 [109].

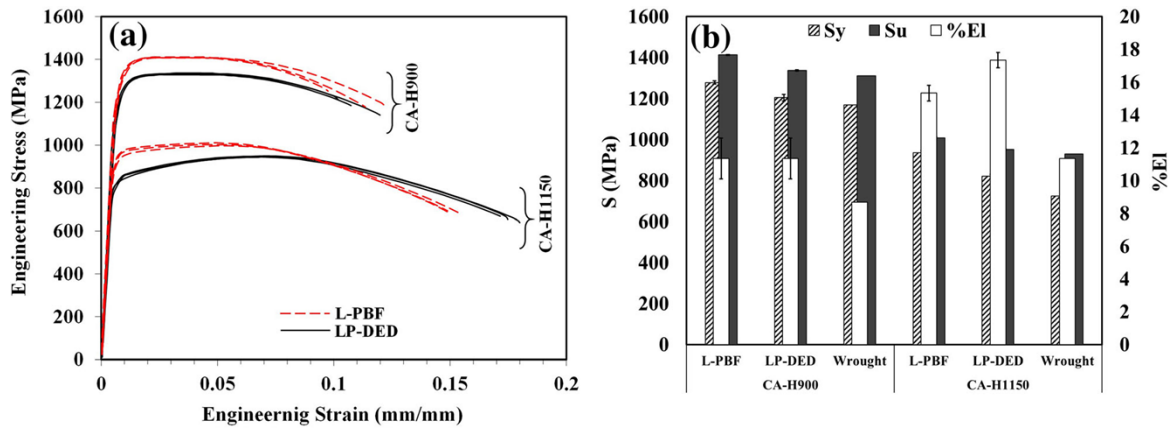


Figure 18: Tensile behaviors of the L-PBF and LP-DED 17-4 PH SS specimens which have undergone CA-H900 and CA-H1150 heat treatment conditions: (a) flow stress curves, (b) summarized tensile properties, and (c) %elongation versus ultimate tensile strength. The wrought data has been taken from ASTM A693 [109]

The fracture surface of the LPBF and LP-DED specimens was also significantly different between the CA-H900 and CA-H1150 heat treatments. Fracture surface of samples subjected to CA-H1150 exhibited larger shear lips with well-defined cup-and-cone features indicative of higher ductility, compared to those subjected to CA-H900, as seen in **Figure 19** [109]. Additionally, CA-H900-treated LP-DED samples were seen to have larger cracks and facets, compared to similarly treated LPBF samples, due to the presence of larger δ -ferrite in the LP-DED microstructure [109].

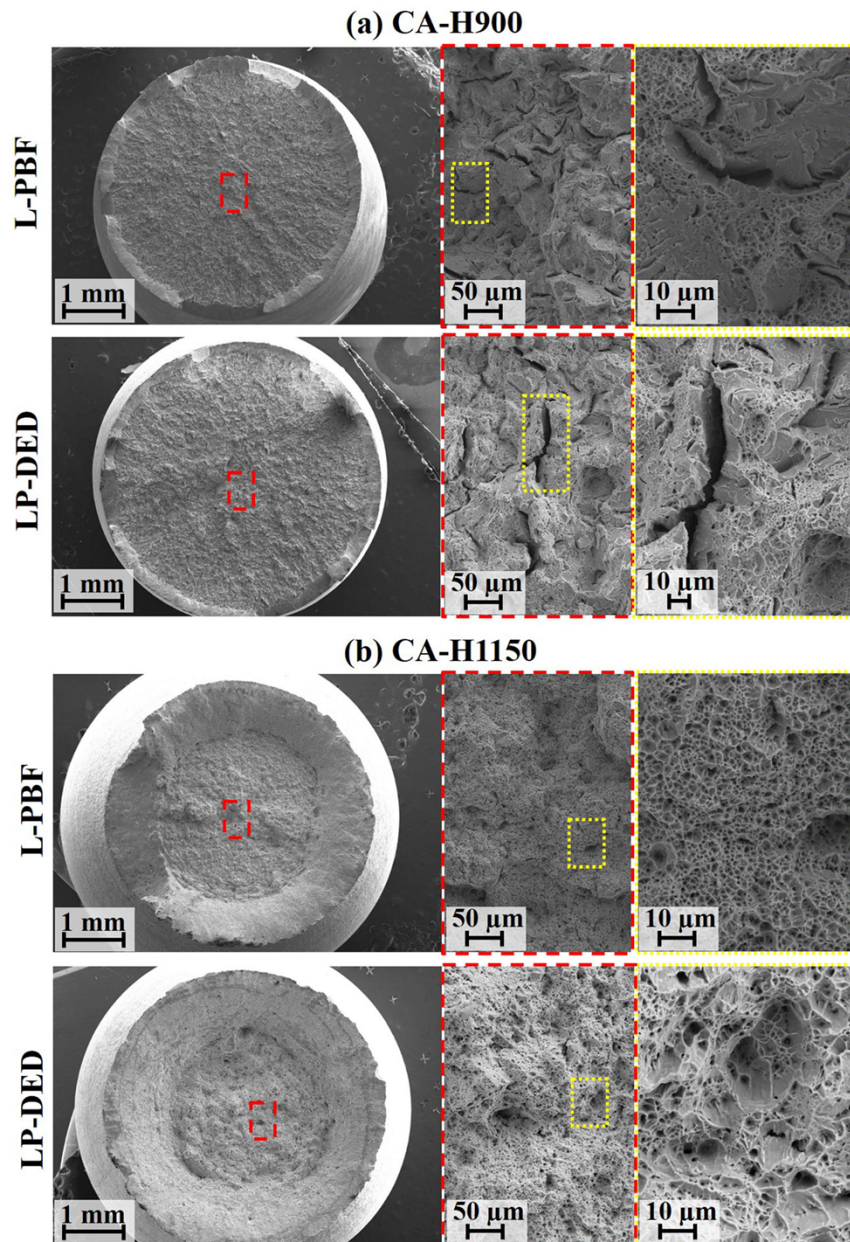


Figure 19: Fractographic analysis of spent tensile samples of DED 17-4PH samples processed under different heat treatment conditions by Nezhadfar et. al.[109]

Most recently in 2024, Mohammadi et. al. [120] investigated the microstructural characteristics, microhardness, and tensile property evolution in $120 \times 70 \times 18$ mm WAAM 17-4 PH walls at different locations along the build and deposition directions (**Figure 20**). It was found that the microstructure of the as-deposited part showed predominantly lathy morphology of δ -ferrite at the bottom and middle of the wall, while vermicular δ -ferrite morphology at the top [120]. Moreover, the volume fraction of retained austenite (20–5%) and δ -ferrite phases (15.5–2.5%) was observed to decrease gradually from the bottom to the top of the as-deposited wall, leading to a progressive increase in both hardness (~37%) and ultimate tensile strength (UTS) along the building direction [120]. Such variations in microstructure and mechanical properties along the build direction was attributed to (1) Differences in cooling rates at locations closer to the substrate due to the ability of the substrate to absorb and dissipate heat, facilitating faster cooling (2) Application of interpass temperature to manage heat input and heat accumulation from prior passes, leading to differences in cooling rates [120].

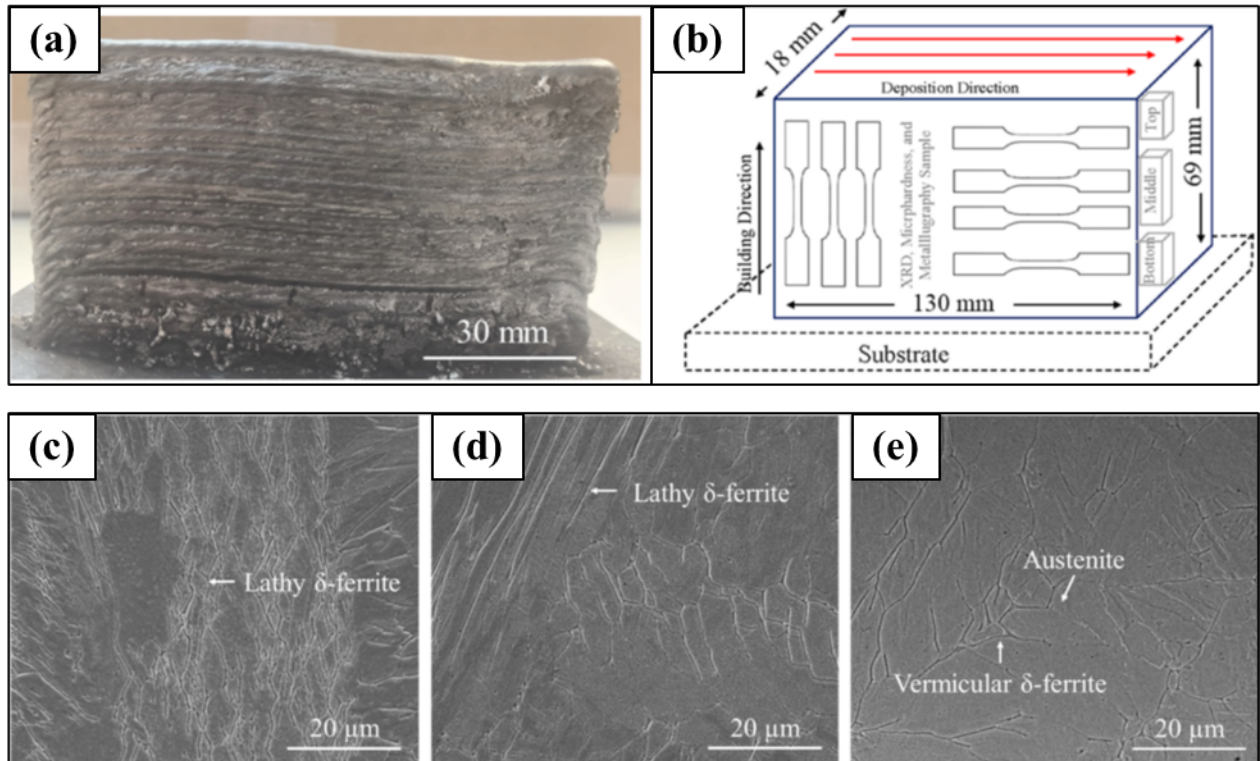


Figure 20: (a) As printed WAAM 17-4 PH sample, (b) build and deposition directions of the sample with respect to the substrate; (c, d, e) SEM images comparing the fraction of δ -ferrite formed in the as built sample at bottom, middle, and top regions of the deposited wall respectively [120].

Tensile testing of samples extracted from the as-printed samples along the build and deposition directions was also performed. Although the average ultimate tensile strength (UTS) of samples extracted from both directions was found to be similar, there was significant anisotropy in % elongation (ductility), with approximately double the ductility along the deposition direction compared to the build direction (**Figure 21(a)**) [120]. The anisotropy in ductility was explained by the differences in directionality of the δ -ferrite grain boundaries along the build direction (**Figure 21(b)**) [120]. Moreover, the differences in tensile properties of horizontal samples

extracted from the top, middle and bottom of the builds was attributed to the amount of δ -ferrite which is a softer and less-ductile phase compared to retained austenite or martensite. Further, evidence of strain hardening (stage II) in horizontal specimen was hypothesized to be due to the presence of high density of dislocation and strain induced austenite to martensite transformation [120], although evidence of these phenomena was not discussed in this paper. Overall, such distinct changes in microstructure and ensuing mechanical properties due to differences in thermal history and cooling rates, emphasizes the significance of toolpath planning and informed parameter selection for feature-based qualification of WAAM deposited 17-4PH stainless steel components.

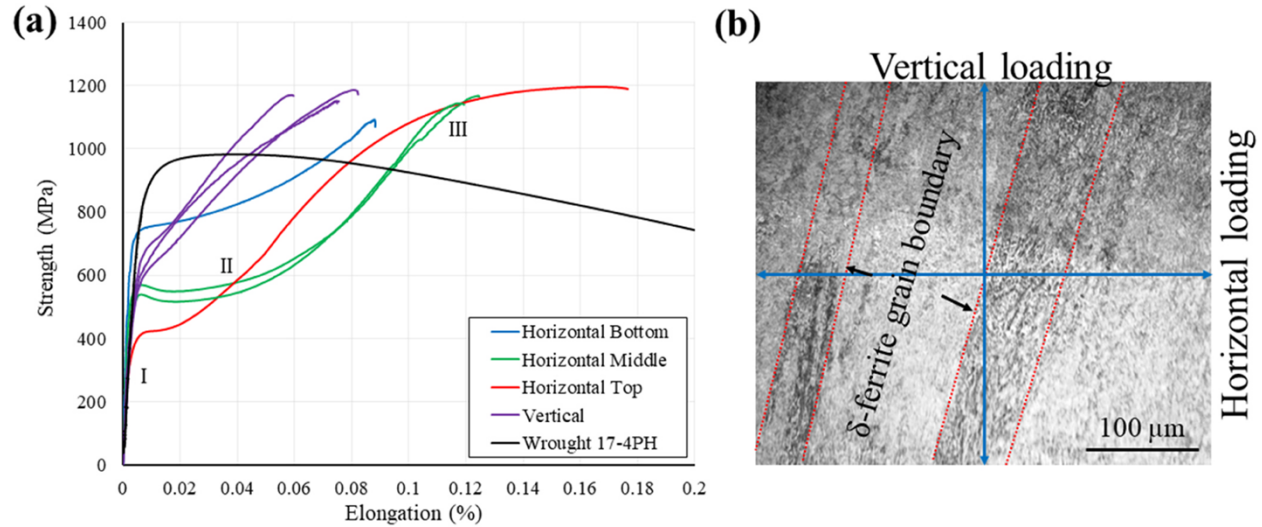


Figure 21: (a) Engineering stress-strain curves of the as-printed wall in the vertical and horizontal directions, and (b) the relative orientation between the tensile loading direction and primary columnar crystals for vertical and horizontal specimen [120].

The phase transformation of 17-4 PH stainless steel alloy is greatly influenced by the cooling rates and temperatures used in various heat treatments. Thus, to achieve optimal microstructures in WAAM stainless steel parts, a comprehensive understanding of solidification behavior and phase transformations in complex WAAM thermal cycles, as well as the relationship between material compositions, process parameters, heat treatment parameters, and the final microstructure, is crucial. Particularly, the thermal history in WAAM processes is seen to have a significant impact on the microstructure, specifically the proportion of retained austenite, martensite, and ferrite phases. Controlling the process parameters allows for the manipulation of the microstructure, specifically in promoting the nucleation and growth of precipitates in δ -ferrite, thereby impacting hardness and mechanical properties of final part [3]. As shown in **Table 7**, SS 17-4PH fabricated by WAAM and/or DED techniques can have a wide range of mechanical properties, based on the print parameters, build conditions, and post-printing heat treatments.

Table 7: A compilation of mechanical properties of as-printed SS 17-4PH alloy fabricated by WAAM and DED modalities by researchers in the past.

Reference	Year	AM Modality	Mechanical Properties			
			Hardness (HV)	Yield Strength (MPa)	UTS (MPa)	% Elongation
[121]	2021	LPBF	300-350	520	1150	8
[122]	2022	LPBF	358-365	N/M	N/M	N/A
[118]	2019	LPBF	N/M	830	887	N/A
[123]	2024	LPBF	426 ± 16	1218 ± 68	1431 ± 5	10 ± 1
[124]	2020	BP-DED	402	N/M	N/M	N/M
[125]	2023	BP-DED	360	937	1008	8
[3]	2019	WAAM	320-340	708-907	966-1064	11.3 – 12.9
[126]	2022	WAAM	325-350	678 ± 3	975 ± 16	11.7 ± 0.1
[120]	2024	WAAM	315-360	636-698	1150-1187	7.2 - 12.5
[120]	2024	Wrought	N/M	954	725	>20

3. QUALIFICATION OF METAL ADDITIVE MANUFACTURED (M-AM) PARTS:

In spite of all the recent advancements in advanced manufacturing tools and additive manufacturing (AM) technologies, AM has not yet fully realized its complete potential. The current lack of process reliability is a significant obstacle to the widespread commercial use of AM technology [17]. Although there is a plethora of information on additive manufacturing (AM) and its related technologies, such as welding, there is still a significant amount of engineering expertise that needs to be explored in order to fulfill the demands of the industrial sector [127]. Consequently, additive manufacturing (AM) has a diverse scope, with collaborative endeavors in software, hardware, and material development aimed at enhancing its competitiveness against established manufacturing alternatives [127]. The primary representative technologies in the area of metal additive manufacturing (M-AM) - Powder Bed Fusion (PBF) and Directed Energy Deposition (DED), are utilized to manufacture components that cannot be produced using traditional subtractive methods [17, 127]. Nevertheless, the additive manufacturing of commercially viable, large-scale, application-based functioning components is still a rarity.

Zhu et al. identified macroscopic mechanical imperfections, such as geometry deviations, and microscopic defects, such as porosity and cracks, as significant barriers to achieving high-quality metal parts via M-AM technologies [128]. Various solutions are being adopted to address the current challenges with incorporating M-AM technologies in production lines of industries. Experimental research can be conducted to refine the design, method, and property windows in order to develop AM knowledge although such an approach that is based on trial and error is both costly and has limited practicality in business environments [127, 129]. On the other hand, the intricate physical phenomena involved in additive manufacturing processes, such as heat transfer, mass transfer, and phase transition, can be accurately represented and studied using physics-based numerical or analytical techniques [130, 131] and has the potential to greatly accelerate the development of processes by focusing on important characteristics of importance. However, the

computational costs, oversimplified assumptions, and lengthier execution times of physics-based approaches may outweigh the potential benefits [132].

To accelerate part production via M-AM it is quintessential to characterize and understand the quality of an additively manufactured component using minimal trial and error experimentation. There are two main methods for assessing the performance of a system: (1) by directly measuring the components or characteristics of the system, and (2) by measuring a test artifact that has been made [133, 134]. Researchers in the past have used benchmark test artifacts for various AM technologies to help evaluate the process feasibility and the part quality. Utilizing test artifacts to assess performance is not exclusive to AM. In fact, many standard artifacts are employed to evaluate the performance of metal cutting machine tools [133, 134]. **Figure 22(a)** is a test artifact commonly called the circle-diamond-square test piece, which is used in the machining industry and was initially specified in 1969 [133].

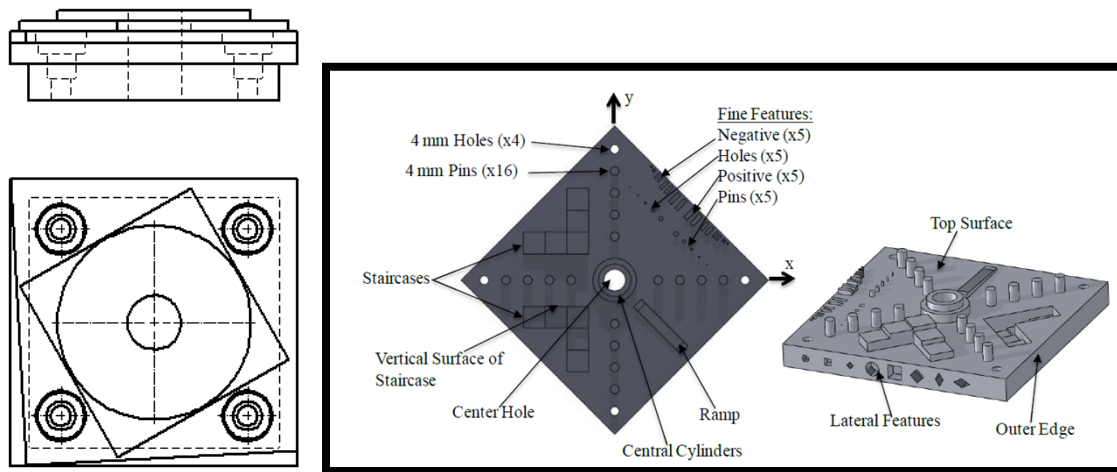


Figure 22: (a) Circle-Diamond square test artifact commonly used in machining industry [134] (b) Test artifact model proposed by Moylan et. al. with arrows pointing to important features in top view (left) and oblique view (right) [133].

Mahesh et. al. [135] initially proposed a categorization of benchmark test artifacts for additive manufacturing (AM) processes into three classes based on their primary objective.

i. Geometrical Benchmark:

These test artifacts are utilized for the purpose of verifying and contrasting the geometrical and dimensional capabilities (such as tolerances, precision, repeatability, and surface polish) of one or more additive manufacturing (AM) systems [136].

ii. Mechanical Benchmark:

These test artifacts enable the characterization of the mechanical properties, such as tensile/compression strength, shrinkage, warping, and creep characteristics, of components produced using a certain additive manufacturing (AM) technology, and are typically developed according to established ASTM standards for evaluating mechanical qualities [136].

iii. Process Benchmark:

These comprise of benchmark artifacts designed to determine the most effective process parameters, such as part orientation, support structures, layer thickness, and speed.

Designing a universal test item for process optimization in additive manufacturing (AM) is exceptionally challenging due to the wide range of working principles underlying AM technologies, therefore emphasizing the need for technology specific benchmarking artifacts [136].

Past researchers have also explored process optimization methodologies using test parts for stereolithography (SL) [137, 138], selective laser sintering (SLS) [139], fused deposition modeling (FDM) [140-143], and multi-jet modeling (MJ) [144]. According to a recent review by Rebaioli et. al. [136], there are over 60 Geometric Benchmark Test Artifacts (GBTA) in literature. The primary objective of printingGBTAs is to forecast and assess the geometric capacity and uncertainties in the additive manufacturing process prior to printing the ultimate product or a fully functional component [145].

Rupal et. al. [146] highlighted the existence of standard test parts (as outlined by ASTM) for mechanical property evaluation, but the lack of clarity in the design and application of Geometric Benchmark Test Artifacts (GBTAs) for the purpose of predicting, assessing, and interpreting geometric features. **Figure 23 (a)** provides an overview of some of the most common output parameters used to test the quality of an AM part. The authors argue that GBTA should not be generalized, but rather tailored to the additive manufacturing (AM) process, the specific application product being considered, or the required geometric assessment metric. In this study, the authors presented a methodical approach for designingGBTAs to assess the geometric performance of AM parts by breaking down intricate geometries into basic implicit features such as cubes, cylinders, and prisms, which have well-defined geometric properties. This simplification aids in selecting the appropriate features based on the desired output, such as Geometric Dimensioning and Tolerancing (GD&T), fit for assembly evaluation, and other geometric properties [146]. Ultimately, a case study is provided to illustrate the approach for developing a GBTA specifically tailored for an application-based product. A case study of the GE LEAP® aviation engine bracket as shown in **Figure 23 (b)** is analyzed, and special suggestions for designing GBTA for this particular application were provided [146].

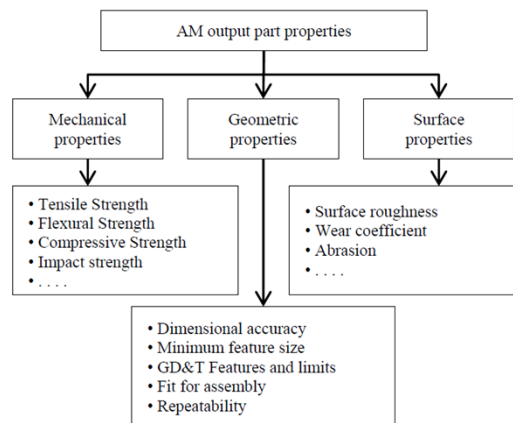


Fig. 1. Overview of AM output part properties

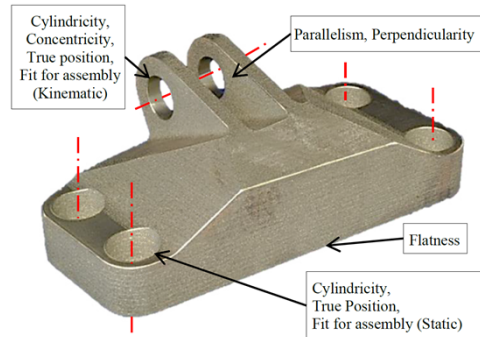


Fig. 3. GE LEAP® aircraft engine bracket (Adapted from [22])

Figure 23: (a) Overview of AM output properties [146] (b) GE LEAP® aviation engine bracket used in this study [146]

The last decade (2014-2024) has seen a growing number of researchers and scientists in the field of additive manufacturing (AM) using empirical models to approach and address AM challenges [127, 147]. These encompass both traditional statistical methods and sophisticated machine learning (ML) and deep learning (DL) techniques [127]. Data-driven methodologies are known to offer several advantages over physics-based analytical or numerical techniques due to their empirical nature as well described by Safdar et. al. [127]. The study by Yang Shi et. al. [145], is a good example of incorporating a novel feature-based approach for conducting manufacturability analysis in additive manufacturing (AM) utilizing the Heat Kernel Signature. This method simultaneously detected geometric features and production constraints to enable a thorough examination from a manufacturing standpoint, facilitating redesign and downstream process planning [145]. Several example component models, including a common a NIST standard test artifact is utilized as an illustration to showcase the practicality of using the suggested approach for feature identification and manufacturability [145].

Later in 2021, Nag et. al. [148] leveraged a hybrid-physics-based multi-objective optimization tool to predict processing-structure-property (PSP) relationships in thin-walls of Ti-6Al-4V built using powder-fed DED technique. Probabilistic ML models were seen to achieve targeted predictions with half the sample space when compared with conventional design of experiments, while also being 37–50% more reliable with respect to regression tools with linear basis function [148]. This work was motivated by the need for feature-based-qualification (FBQ) methodology to decompose a complex structure such as a conceptual component (**Figure 24**) that imitates a standard pressure casing utilized in gas turbines, by identifying critical performance-limiting features, while reducing the cost and time of DED process qualification [148]. The objective was to assess the impact of print parameters on the microstructure and mechanical characteristics of DED Ti-6Al-4V thin walls, where the resulting data was utilized to train a Bayesian hybrid model [148]. This work stands out to be the only study known to the authors, that focusses on feature-based-qualification of components printed using directed energy deposition (DED) additive manufacturing modality.

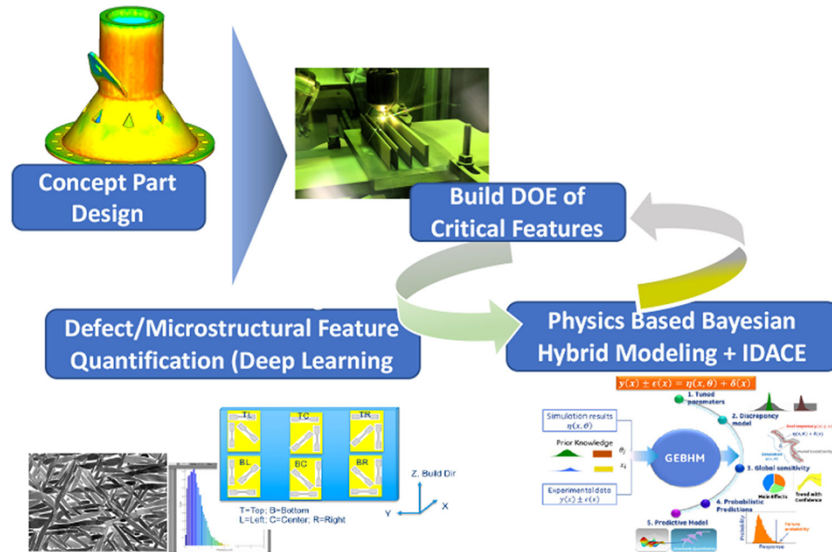








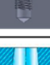



Figure 24: FBQ methodology suggested by Nag et. al. showing a concept part, selection of critical feature builds, and using quantitative characterization to generate physics-based Bayesian hybrid models [148]

More recently in 2023, Kashouty et. al. [149] explored the creation of a feature-based manufacturability assessment system (FBMAS) to showcase the possibility of combining selective laser melting (SLM), with subtractive manufacturing for every given part. An FBMAS graphical user interface (GUI) is developed using a structural approach, which is explained in detail to ensure effective and user-friendly operation [149]. The established systematic approach effectively harnesses the advantages of SLM and subtractive manufacturing technologies, while clearly delineating the design constraints associated with each production method [149]. The authors outlined design features from the literature, that helped guide this work on FBMAS for additive and subtractive manufacturing technologies (**Table 8**) [149].

Table 8: List of design features, definition of each feature, and sample illustrations outlined by Kashouty et. al. based on past literature [149].

Design Feature	Illustration	Comments
Hole		A hole originates from a rounded profile. Typically includes 'through', 'blind', and 'tapered' holes
Slot		A slot is a perimeter that has a constant center line and width. Typically includes 'blind' (contoured with two ends) and 'through' (passes completely through the part)
Pocket		Feature with an open/closed perimeter (open pocket or closed pocket). Includes 'through' and 'blind'
Boss Extrude		This feature adds to the area of the surface through extrusion above the planar surface
Freeform Pattern/		Multiple iterations of the same feature, grouped together to create a pattern, that can be machined as individual features or as a pattern
Fillet		Rounded corners or a curve created at the intersection of two or more faces
Sharp Edge		Sharp edge on the external side of a body
Undercut		Non-visible recessed surface that is inaccessible using a straight tool
Tapping		Usually responsible for creating screw threads in a hole
Negative Draft		In a part viewed from a plan view, the side walls are tapered towards the bottom; the internal dimension at the bottom has a larger dimension compared to the top

Additive Manufacturing (AM) undoubtedly offers increased flexibility in terms of how a product can be manufactured when compared to conventional manufacturing techniques. During the process phase, this freedom is typically manifested through a choice of various deposition techniques, build orientations, and support configurations that can be adjusted to print a certain geometry or a feature, and will later determine the micro- and macro-characteristics of the final printed part [127, 150]. Hence, it is necessary to streamline and simplify the intricate design process before employing AM as a widespread production method for specific applications.

4. CONCLUSION

Currently, it can take several years to go from part concept to production on mission critical AM components. This delay is incredibly prohibitive to the broad adoption of AM technologies for use in sustainment applications, such as heat exchangers and fuel nozzles where cost and readiness are vital to the acquisition process. The AM product qualification timeline is comprised of design engineering and supply chain substantiation and development, but the longest task in the timeline is authentication. Process substantiation in the past has been an extremely iterative cycle of preparing builds, printing parts, post-processing, conducting dimensional inspection, material performance evaluation, and functional performance evaluation. Component performance includes both form and function—relative to the requirements—during design, operation, and sustainment. That is, it needs to perform its intended function and do so for a sustained and predictable period of life. Developing the complex processing-microstructure-performance understanding and relations are time consuming for the needs these components fulfill in current designs. The Feature Based Qualification (FBQ) methodology does enable more efficient design of components targeted for AM part production by providing the engineering community with a feature-based performance and property data tool. This methodology leverages experimental trials with user defined geometric features from which the mechanical properties and microstructural characteristics of broader example parts can be readily predicted. Manufacturing engineers may employ the feature-based process when preparing a component build and use the FBQ methodology to define the qualification work scope, testing requirements, and acceptance criteria. The project will help understand the correlation between build process parameters, build geometry and mechanical performance for 17-4PH alloy.

REFERENCES:

1. Thompson, S.M., et al., *An overview of Direct Laser Deposition for additive manufacturing; Part I: Transport phenomena, modeling and diagnostics*. Additive Manufacturing, 2015. **8**: p. 36-62.
 2. Shamsaei, N., et al., *An overview overview of Direct Laser Deposition for additive manufacturing; Part II: Mechanical behavior, process parameter optimization and control*. Additive Manufacturing, 2015. **8**: p. 12-35.
 3. Caballero, A., et al., *Wire plus Arc Additive Manufacture of 17-4 PH stainless steel: Effect of different processing conditions on microstructure, hardness, and tensile strength*. Journal of Materials Processing Technology, 2019. **268**: p. 54-62.
 4. Jin, W.W., et al., *Wire Arc Additive Manufacturing of Stainless Steels: A Review*. Applied Sciences-Basel, 2020. **10**(5).
 5. Ding, D.H., et al., *A multi-bead overlapping model for robotic wire and arc additive manufacturing (WAAM)*. Robotics and Computer-Integrated Manufacturing, 2015. **31**: p. 101-110.
 6. Chen, B. and J. Mazumder, *Role of process parameters during additive manufacturing by direct metal deposition of Inconel 718*. Rapid Prototyping Journal, 2017. **23**(5): p. 919-929.
 7. Yusuf, S.M., S. Cutler, and N. Gao, *Review: The Impact of Metal Additive Manufacturing on the Aerospace Industry*. Metals, 2019. **9**(12).
-

8. Seede, R., et al., *An ultra-high strength martensitic steel fabricated using selective laser melting additive manufacturing: Densification, microstructure, and mechanical properties*. Acta Materialia, 2020. **186**: p. 199-214.
 9. Martina, F., et al., *Tandem metal inert gas process for high productivity wire arc additive manufacturing in stainless steel*. Additive Manufacturing, 2019. **25**: p. 545-550.
 10. Available from: <https://ampower.eu/infographics/metal-additive-manufacturing/>.
 11. Ngo, T.D., et al., *Additive manufacturing (3D printing): A review of materials, methods, applications and challenges*. Composites Part B-Engineering, 2018. **143**: p. 172-196.
 12. Rodrigues, T.A., et al., *Current Status and Perspectives on Wire and Arc Additive Manufacturing (WAAM)*. Materials, 2019. **12**(7).
 13. Thapliyal, S., *Challenges associated with the wire arc additive manufacturing (WAAM) of aluminum alloys*. Materials Research Express, 2019. **6**(11).
 14. Albannai, A.I., *A brief review on the common defects in wire arc additive manufacturing*. Int. J. Curr. Sci. Res. Rev, 2022. **5**: p. 4556-4576.
 15. Ghaffari, M., A. Vahedi Nemani, and A. Nasiri, *Microstructure and mechanical behavior of PH 13-8Mo martensitic stainless steel fabricated by wire arc additive manufacturing*. Additive Manufacturing, 2022. **49**: p. 102374.
 16. Queguineur, A., et al., *Wire arc additive manufacturing of thin and thick walls made of duplex stainless steel*. International Journal of Advanced Manufacturing Technology, 2023. **127**(1-2): p. 381-400.
 17. Frazier, W.E., *Metal Additive Manufacturing: A Review*. Journal of Materials Engineering and Performance, 2014. **23**(6): p. 1917-1928.
 18. McAndrew, A.R., et al., *Interpass rolling of Ti-6Al-4V wire + arc additively manufactured features for microstructural refinement*. Additive Manufacturing, 2018. **21**: p. 340-349.
 19. Xiong, J. and G.J. Zhang, *Adaptive control of deposited height in GMAW-based layer additive manufacturing*. Journal of Materials Processing Technology, 2014. **214**(4): p. 962-968.
 20. Zhang, H.T., et al., *The arc characteristics and metal transfer behaviour of cold metal transfer and its use in joining aluminium to zinc-coated steel*. Materials Science and Engineering a-Structural Materials Properties Microstructure and Processing, 2009. **499**(1-2): p. 111-113.
 21. Posch, G., K. Chladil, and H. Chladil, *Material properties of CMT-metal additive manufactured duplex stainless steel blade-like geometries*. Welding in the World, 2017. **61**(5): p. 873-882.
 22. Zhang, Y.M., et al., *Weld deposition-based rapid prototyping: a preliminary study*. Journal of Materials Processing Technology, 2003. **135**(2-3): p. 347-357.
 23. Ding, D.H., et al., *Wire-feed additive manufacturing of metal components: technologies, developments and future interests*. International Journal of Advanced Manufacturing Technology, 2015. **81**(1-4): p. 465-481.
 24. Bellamkonda, P.N., M. Dwivedy, and R. Addanki, *Cold metal transfer technology - A review of recent research developments*. Results in Engineering, 2024. **23**.
 25. Imoudu, N.E., Y.Z. Ayele, and A. Barabadi, *The Characteristic of Cold Metal Transfer (CMT) and its Application for Cladding*. 2017 Ieee International Conference on Industrial Engineering and Engineering Management (Ieem), 2017: p. 1883-1887.
-

26. Tomar, B. and S. Sekar, *Cold metal transfer-based wire arc additive manufacturing of pure copper with ultra high tensile strength*. Proceedings of the Institution of Mechanical Engineers Part E-Journal of Process Mechanical Engineering, 2024.
 27. Ding, J., et al., *Thermo-mechanical analysis of Wire and Arc Additive Layer Manufacturing process on large multi-layer parts*. Computational Materials Science, 2011. **50**(12): p. 3315-3322.
 28. Aiyiti, W., et al., *Investigation of the overlapping parameters of MPAW-based rapid prototyping*. Rapid Prototyping Journal, 2006. **12**(3): p. 165-172.
 29. Han, S.W., et al., *Plasma Arc Welding of 780CP High Strength Steel Sheet Lap Joint for Tensile Strength of 100% Compared to Base Metal*. International Journal of Precision Engineering and Manufacturing, 2024. **25**(5): p. 925-931.
 30. Jiang, F., et al., *A novel optimizing Pulsed Plasma Gas Variable Polarity Plasma Arc Welding (PPG-VPPAW) method for improving weld quality*. Journal of Materials Processing Technology, 2024. **327**.
 31. Zhou, F.Z., et al., *Better generalization of penetration/keyhole status prediction model in plasma arc welding based on UDAs: A preliminary work*. Journal of Manufacturing Processes, 2024. **124**: p. 985-997.
 32. Williams, S.W., et al., *Wire plus Arc Additive Manufacturing*. Materials Science and Technology, 2016. **32**(7): p. 641-647.
 33. Wu, B.T., et al., *The anisotropic corrosion behaviour of wire arc additive manufactured Ti-6Al-4V alloy in 3.5% NaCl solution*. Corrosion Science, 2018. **137**: p. 176-183.
 34. Gu, J.L., et al., *The strengthening effect of inter-layer cold working and post-deposition heat treatment on the additively manufactured Al-6.3Cu alloy*. Materials Science and Engineering a-Structural Materials Properties Microstructure and Processing, 2016. **651**: p. 18-26.
 35. Zou, X.D., et al., *Wire plus Arc Additive Manufacturing and Heat Treatment of Super Martensitic Stainless Steel with a Refined Microstructure and Excellent Mechanical Properties*. Materials, 2022. **15**(7).
 36. Xu, F.J., et al., *Microstructural Evolution and Mechanical Properties of Inconel 625 Alloy during Pulsed Plasma Arc Deposition Process*. Journal of Materials Science & Technology, 2013. **29**(5): p. 480-488.
 37. Bhaduri, A.K., et al., *Optimized postweld heat treatment procedures for 17-4 PH stainless steels*. Welding Journal, 1995. **74**: p. Medium: X; Size: pp. 153.s-159.s 2009-12-16.
 38. Vagi, J.J., R.M. Evans, and D.C. Martin, *Welding of Precipitation-Hardening Stainless Steels*. 1968: United States.
 39. Wu, B.T., et al., *A review of the wire arc additive manufacturing of metals: properties, defects and quality improvement*. Journal of Manufacturing Processes, 2018. **35**: p. 127-139.
 40. Herzog, D., et al., *Additive manufacturing of metals*. Acta Materialia, 2016. **117**: p. 371-392.
 41. Lippold, J.C., *Recent developments in the understanding of stainless steel welding metallurgy*. Trends in Welding Research, Proceedings, 2003: p. 1-10.
 42. Baufeld, B., O. van der Biest, and R. Gault, *Microstructure of Ti-6Al-4V specimens produced by shaped metal deposition*. International Journal of Materials Research, 2009. **100**(11): p. 1536-1542.
-

43. Albannai, A.I., *A Brief Review on The Common Defects in Wire Arc Additive Manufacturing*. International Journal of Current Science Research and Review, 2022. **Vol 5 No 12**.
 44. Tabernero, I., et al., *Study on Arc Welding processes for High Deposition Rate Additive Manufacturing*. 19th Cirp Conference on Electro Physical and Chemical Machining, 2018. **68**: p. 358-362.
 45. Fu, R., et al., *Hot-wire arc additive manufacturing of aluminum alloy with reduced porosity and high deposition rate*. Materials & Design, 2021. **199**.
 46. Wang, D.H., et al., *Reducing Porosity and Refining Grains for Arc Additive Manufacturing Aluminum Alloy by Adjusting Arc Pulse Frequency and Current*. Materials, 2018. **11**(8).
 47. Derekar, K.S., et al., *Effect of pulsed metal inert gas (pulsed-MIG) and cold metal transfer (CMT) techniques on hydrogen dissolution in wire arc additive manufacturing (WAAM) of aluminium*. International Journal of Advanced Manufacturing Technology, 2020. **107**(1-2): p. 311-331.
 48. Bai, J., et al., *Porosity evolution in additively manufactured aluminium alloy during high temperature exposure*. 1st International Conference on New Material and Chemical Industry (Nmci2016), 2017. **167**.
 49. Fang, X.W., et al., *Microstructure evolution of wire-arc additively manufactured 2319 aluminum alloy with interlayer hammering*. Materials Science and Engineering a-Structural Materials Properties Microstructure and Processing, 2021. **800**.
 50. Ghaffari, M., et al., *Effect of Solidification Defects and HAZ Softening on the Anisotropic Mechanical Properties of a Wire Arc Additive-Manufactured Low-Carbon Low-Alloy Steel Part*. Jom, 2019. **71**(11): p. 4215-4224.
 51. Mukherjee, T. and T. DebRoy, *Mitigation of lack of fusion defects in powder bed fusion additive manufacturing*. Journal of Manufacturing Processes, 2018. **36**: p. 442-449.
 52. Marinelli, G., et al., *Development of Wire plus Arc additive manufacture for the production of large-scale unalloyed tungsten components*. International Journal of Refractory Metals & Hard Materials, 2019. **82**: p. 329-335.
 53. Murali, N., et al., *Gas-Tungsten Arc Welding of Dissimilar Aluminum Alloys With Nano-Treated Filler*. Journal of Manufacturing Science and Engineering-Transactions of the Asme, 2021. **143**(8).
 54. Zhang, G.J., C.Y. Xiao, and M. Taheri, *Effect of Nd:YAG pulsed laser welding process on the liquation and strain-age cracking in GTD-111 superalloy*. Journal of Manufacturing Processes, 2020. **52**: p. 66-78.
 55. Albannai, A., et al., *Effects of Tandem Side-by-side GTAW Welds on Centerline Solidification Cracking of AA2024*. Manufacturing Technology, 2021. **21**(2): p. 150-162.
 56. Langelandsvik, G., et al., *Review of Aluminum Alloy Development for Wire Arc Additive Manufacturing*. Materials, 2021. **14**(18).
 57. Kang, M., H.N. Han, and C. Kim, *Microstructure and Solidification Crack Susceptibility of Al 6014 Molten Alloy Subjected to a Spatially Oscillated Laser Beam*. Materials, 2018. **11**(4).
 58. Kou, S. and Y. Le, *Grain-Structure and Solidification Cracking in Oscillated Arc Welds of 5052 Aluminum-Alloy*. Metallurgical Transactions a-Physical Metallurgy and Materials Science, 1985. **16**(7): p. 1345-1352.
-

59. Albannai, A.I., et al., *Improving Centerline Solidification Crack Resistivity of AA 2024 Using Tandem Side-by-Side GTAW Technique*. Materials Performance and Characterization, 2019. **8**(4): p. 541-554.
 60. Yu, P., J. Morrow, and S. Kou, *Resistance of Austenitic Stainless Steels to Ductility-Dip Cracking: Mechanisms*. Welding Journal, 2021. **100**(9): p. 291s-301s.
 61. Chen, Y., et al., *Characterization of heat affected zone liquation cracking in laser additive manufacturing of Inconel 718*. Materials & Design, 2016. **90**: p. 586-594.
 62. Vimal, K.E.K., M.N. Srinivas, and S. Rajak, *Wire arc additive manufacturing of aluminium alloys: A review*. Materials Today-Proceedings, 2021. **41**: p. 1139-1145.
 63. Bermingham, M.J., et al., *Optimising the mechanical properties of Ti-6Al-4V components produced by wire plus arc additive manufacturing with post-process heat treatments*. Journal of Alloys and Compounds, 2018. **753**: p. 247-255.
 64. Ravisankar, A., et al., *Influence of welding speed and power on residual stress during gas tungsten arc welding (GTAW) of thin sections with constant heat input: A study using numerical simulation and experimental validation*. Journal of Manufacturing Processes, 2014. **16**(2): p. 200-211.
 65. Vazquez, L., et al., *Influence of Post-Deposition Heat Treatments on the Microstructure and Tensile Properties of Ti-6Al-4V Parts Manufactured by CMT-WAAM*. Metals, 2021. **11**(8).
 66. Hönnige, J.R., et al., *Control of residual stress and distortion in aluminium wire plus arc additive manufacture with rolling*. Additive Manufacturing, 2018. **22**: p. 775-783.
 67. Sun, R.J., et al., *Microstructure, residual stress and tensile properties control of wire-arc additive manufactured 2319 aluminum alloy with laser shock peening*. Journal of Alloys and Compounds, 2018. **747**: p. 255-265.
 68. Shen, C., et al., *Neutron diffraction residual stress determinations in Fe₃Al based iron aluminide components fabricated using wire-arc additive manufacturing (WAAM)*. Additive Manufacturing, 2019. **29**.
 69. Biserova-Tahchieva, A., et al., *Additive Manufacturing Processes in Selected Corrosion Resistant Materials: A State of Knowledge Review*. Materials, 2023. **16**(5).
 70. Shah, A., et al., *A Review of the Recent Developments and Challenges in Wire Arc Additive Manufacturing (WAAM) Process*. Journal of Manufacturing and Materials Processing, 2023. **7**(3): p. 97.
 71. Belhadj, M., et al., *Effect of cold metal transfer-based wire arc additive manufacturing parameters on geometry and machining allowance*. The International Journal of Advanced Manufacturing Technology, 2024. **131**(2): p. 739-748.
 72. Alomari, Y., M.T. Biroş, and M. Andó, *Part orientation optimization for Wire and Arc Additive Manufacturing process for convex and non-convex shapes*. Scientific Reports, 2023. **13**(1): p. 2203.
 73. Ji, L., et al., *Research on Mechanisms and Controlling Methods of Macro Defects in TC4 Alloy Fabricated by Wire Additive Manufacturing*. Materials, 2018. **11**(7): p. 1104.
 74. Brennan, M.C., J.S. Keist, and T.A. Palmer, *Defects in Metal Additive Manufacturing Processes*. Journal of Materials Engineering and Performance, 2021. **30**(7): p. 4808-4818.
 75. Lopez, A., et al., *Non-destructive testing application of radiography and ultrasound for wire and arc additive manufacturing*. Additive Manufacturing, 2018. **21**: p. 298-306.
-

76. Gordon, J.V. and D.G. Harlow, *Statistical Modeling of Wire and Arc Additive Manufactured Stainless Steel 304: Microstructure and Fatigue*. International Journal of Reliability Quality and Safety Engineering, 2019. **26**(4).
 77. Lee, Y., et al., *Effect of Interlayer Cooling Time, Constraint and Tool Path Strategy on Deformation of Large Components Made by Laser Metal Deposition with Wire*. Applied Sciences-Basel, 2019. **9**(23).
 78. Kumar, P. and K. Maji, *Experimental investigations and parametric effects on depositions of super duplex stainless steel in wire arc additive manufacturing*. Proceedings of the Institution of Mechanical Engineers Part E-Journal of Process Mechanical Engineering, 2023.
 79. Zhang, Y.Q., F.J. Cheng, and S.J. Wu, *The microstructure and mechanical properties of duplex stainless steel components fabricated via flux-cored wire arc-additive manufacturing*. Journal of Manufacturing Processes, 2021. **69**: p. 204-214.
 80. Hejripour, F., et al., *Thermal modeling and characterization of wire arc additive manufactured duplex stainless steel*. Journal of Materials Processing Technology, 2019. **272**: p. 58-71.
 81. Sülzter, J., et al., *GMAW Cold Wire Technology for Adjusting the Ferrite-Austenite Ratio of Wire and Arc Additive Manufactured Duplex Stainless Steel Components*. Metals, 2019. **9**(5).
 82. DebRoy, T., et al., *Additive manufacturing of metallic components - Process, structure and properties*. Progress in Materials Science, 2018. **92**: p. 112-224.
 83. Jacob, G., *Prediction of Solidification Phases in Cr-Ni Stainless Steel Alloys Manufactured by Laser Based Powder Bed Fusion Process*. 2018, Advanced Manufacturing Series (NIST AMS), National Institute of Standards and Technology, Gaithersburg, MD.
 84. Abrahams, R.A., *The development of high strength corrosion resistant precipitation hardening cast steels*. 2010.
 85. Lu, Y., H.X. Yu, and R.D. Sisson, *The effect of carbon content on the c/a ratio of as-quenched martensite in Fe-C alloys*. Materials Science and Engineering a-Structural Materials Properties Microstructure and Processing, 2017. **700**: p. 592-597.
 86. Shimizu, K. and Z. Nishiyama, *Electron-Microscopic Studies of Martensitic Transformations in Iron-Alloys and Steels*. Metallurgical Transactions, 1972. **3**(5): p. 1055-+.
 87. Hsiao, C.N., C.S. Chiou, and J.R. Yang, *Aging reactions in a 17-4 PH stainless steel*. Materials Chemistry and Physics, 2002. **74**(2): p. 134-142.
 88. Viswanathan, U.K., S. Banerjee, and R. Krishnan, *Effects of Aging on the Microstructure of 17-4 Ph Stainless-Steel*. Materials Science and Engineering a-Structural Materials Properties Microstructure and Processing, 1988. **104**: p. 181-189.
 89. Schulze, G., *Die Metallurgie des Schweißens*. 2009: Springer Berlin, Heidelberg.
 90. Schaeffler, A.L., *Constitution Diagram for Stainless-Steel Weld Metal .2. Schaeffler Diagram*. Metal Progress, 1974. **106**(1): p. 227-227.
 91. Delong, W.T., *Ferrite in Austenitic Stainless-Steel Weld Metal*. Welding Journal, 1974. **53**(7): p. S273-S286.
 92. Kotecki, D.J., *Some Pitfalls in Welding of Duplex Stainless Steels*. Soldagem & Inspecao, 2010. **15**(4): p. 336-343.
-

93. Kotecki, D.J. and T.A. Siewert, *Wrc-1992 Constitution Diagram for Stainless-Steel Weld Metals - a Modification of the Wrc-1988 Diagram*. Welding Journal, 1992. **71**(5): p. S171-S178.
 94. Balmforth, M.C. and J.C. Lippold, *A preliminary ferritic-martensitic stainless steel constitution diagram*. Welding Journal, 1998. **77**(1): p. 1s-7s.
 95. Danoix, F. and P. Auger, *Atom probe studies of the Fe-Cr system and stainless steels aged at intermediate temperature: A review*. Materials Characterization, 2000. **44**(1-2): p. 177-201.
 96. Goodman, S.R., S.S. Brenner, and J.R. Low, *Fim-Atom Probe Study of Precipitation of Copper from Iron-1.4 at Pct Copper .I. Field-Ion Microscopy*. Metallurgical Transactions, 1973. **4**(10): p. 2363-2369.
 97. Isheim, D., et al., *Interfacial segregation at Cu-rich precipitates in a high-strength low-carbon steel studied on a sub-nanometer scale*. Acta Materialia, 2006. **54**(3): p. 841-849.
 98. Murayama, M., Y. Katayama, and K. Hono, *Microstructural evolution in a 17-4 PH stainless steel after aging at 400°C*. Metallurgical and Materials Transactions a-Physical Metallurgy and Materials Science, 1999. **30**(2): p. 345-353.
 99. Wu, J.H. and C.K. Lin, *Influence of high temperature exposure on the mechanical behavior and microstructure of 17-4 PH stainless steel*. Journal of Materials Science, 2003. **38**(5): p. 965-971.
 100. Rack, H.J. and D. Kalish, *Strength, Fracture Toughness, and Low-Cycle Fatigue Behavior of 17-4 Ph Stainless-Steel*. Metallurgical Transactions, 1974. **5**(7): p. 1595-1605.
 101. Bressan, J.D., et al., *Influence of hardness on the wear resistance of 17-4 PH stainless steel evaluated by the pin-on-disc testing*. Journal of Materials Processing Technology, 2008. **205**(1-3): p. 353-359.
 102. Ziewiec, A., J. Czech, and E. Tasak, *Welded Joint Cracking in Martensitic Stainless Steel Precipitation-Strengthened with Copper*. Archives of Metallurgy and Materials, 2012. **57**(4): p. 1055-1061.
 103. Ziewiec, A., A. Zielinska-Lipiec, and E. Tasak, *MICROSTRUCTURE OF WELDED JOINTS OF X5CrNiCuNb16-4 (17-4 PH) MARTENSITIC STAINLESS STEEL AFTER HEAT TREATMENT*. Archives of Metallurgy and Materials, 2014. **59**(3): p. 965-970.
 104. Bhaduri, A.K. and S. Venkadesan, *Microstructure of the Heat-Affected Zone in 17-4 Ph Stainless-Steel*. Steel Research, 1989. **60**(11): p. 509-513.
 105. Das, C.R., et al., *Weldability of 17-4PH stainless steel in overaged heat treated condition*. Science and Technology of Welding and Joining, 2006. **11**(5): p. 502-508.
 106. Agilan, M., et al., *Effect of Post Weld Heat Treatment on Mechanical Properties and Microstructure of Nickel based Super Alloy Welds*. Advances in Materials and Processing: Challenges and Opportunities, 2012. **585**: p. 435-439.
 107. Hamlin, R.J., *Investigation of precipitation and hardening response of maraging stainless steels 17-4 and 13-8+Mo during multi-pass welding*. 2017, Lehigh University: United States -- Pennsylvania. p. 130.
 108. Zhao, H., et al., *Automated image mapping and quantification of microstructure heterogeneity in additive manufactured Ti6Al4V*. Materials Characterization, 2019. **147**: p. 131-145.
 109. Nezhadfar, P.D., et al., *Microstructure and Deformation Behavior of Additively Manufactured 17-4 Stainless Steel: Laser Powder Bed Fusion vs. Laser Powder Directed Energy Deposition*. Jom, 2022. **74**(3): p. 1136-1148.
-

110. Zähr, J., et al., *Numerical and Experimental Studies of the Influence of Process Gases in Tic Welding*. Welding in the World, 2012. **56**(3-4): p. 85-92.
 111. Colaço, R. and R. Vilar, *Stabilisation of retained austenite in laser surface melted tool steels*. Materials Science and Engineering a-Structural Materials Properties Microstructure and Processing, 2004. **385**(1-2): p. 123-127.
 112. Yoo, W.D., et al., *Study on the microstructure and mechanical properties of 17-4 PH stainless steel depending on heat treatment and aging time*. Heat Treatment of Materials, 2006. **118**: p. 15-+.
 113. Xiong, J., Y.Y. Lei, and R. Li, *Finite element analysis and experimental validation of thermal behavior for thin-walled parts in GMAW-based additive manufacturing with various substrate preheating temperatures*. Applied Thermal Engineering, 2017. **126**: p. 43-52.
 114. Das, A. and S. Tarafder, *Geometry of dimples and its correlation with mechanical properties in austenitic stainless steel*. Scripta Materialia, 2008. **59**(9): p. 1014-1017.
 115. Facchini, L., et al., *Metastable Austenite in 17-4 Precipitation-Hardening Stainless Steel Produced by Selective Laser Melting*. Advanced Engineering Materials, 2010. **12**(3): p. 184-188.
 116. LeBrun, T., et al., *Effect of retained austenite on subsequent thermal processing and resultant mechanical properties of selective laser melted 17-4 PH stainless steel*. Materials & Design, 2015. **81**: p. 44-53.
 117. Alnajjar, M., et al., *Evidence of austenite by-passing in a stainless steel obtained from laser melting additive manufacturing*. Additive Manufacturing, 2019. **25**: p. 187-195.
 118. Nezhadfar, P.D., et al., *Fatigue behavior of additively manufactured 17-4 PH stainless steel: Synergistic effects of surface roughness and heat treatment*. International Journal of Fatigue, 2019. **124**: p. 188-204.
 119. Celada-Casero, C., J. Sietsma, and M.J. Santofimia, *The role of the austenite grain size in the martensitic transformation in low carbon steels*. Materials & Design, 2019. **167**.
 120. Mohammadi, J., et al., *Microstructure and mechanical properties of 17-4 PH stainless steel fabricated by gas metal wire arc additive manufacturing*. Materials Today Communications, 2024. **39**.
 121. Sabooni, S., et al., *Laser powder bed fusion of 17-4 PH stainless steel: A comparative study on the effect of heat treatment on the microstructure evolution and mechanical properties*. Additive Manufacturing, 2021. **46**.
 122. Moyle, M.S., et al., *Evidence of Cu clustering as a function of laser power during laser powder bed fusion of 17-4 PH stainless steel*. Scripta Materialia, 2022. **219**.
 123. Sabzi, H.E., et al., *Genetic design of precipitation-hardening stainless steels for additive manufacturing*. Acta Materialia, 2024. **274**: p. 120018.
 124. Mathoho, I., et al., *Impact of DED process parameters on the metallurgical characteristics of 17-4 PH SS deposited using DED*. Cirp Journal of Manufacturing Science and Technology, 2020. **31**: p. 450-458.
 125. Muslim, T., et al., *Laser metal deposition of 17-4 PH stainless steel: Geometrical, microstructural, and mechanical properties investigation for structural applications*. Cirp Journal of Manufacturing Science and Technology, 2023. **41**: p. 69-79.
 126. Zhou, T., et al., *Microstructure control during deposition and post-treatment to optimize mechanical properties of wire-arc additively manufactured 17-4 PH stainless steel*. Additive Manufacturing, 2022. **58**.
-

127. Mutahar Safdar , G.L., Padma Polash Paul , Gentry Wood , Yaoyao Fiona Zhao, *Engineering of Additive Manufacturing Features for Data-Driven Solutions*. 2023: Springer Nature Switzerland.
 128. Zhu, K., J.Y.H. Fuh, and X. Lin, *Metal-Based Additive Manufacturing Condition Monitoring: A Review on Machine Learning Based Approaches*. Ieee-Asme Transactions on Mechatronics, 2022. **27**(5): p. 2495-2510.
 129. Johnson, N.S., et al., *Invited review: Machine learning for materials developments in metals additive manufacturing*. Additive Manufacturing, 2020. **36**.
 130. Luo, Z.B. and Y.Y. Zhao, *A survey of finite element analysis of temperature and thermal stress fields in powder bed fusion Additive Manufacturing*. Additive Manufacturing, 2018. **21**: p. 318-332.
 131. Guan, X.Y. and Y.F. Zhao, *Modeling of the laser powder-based directed energy deposition process for additive manufacturing: a review*. International Journal of Advanced Manufacturing Technology, 2020. **107**(5-6): p. 1959-1982.
 132. Francois, M.M., et al., *Modeling of additive manufacturing processes for metals: Challenges and opportunities*. Current Opinion in Solid State & Materials Science, 2017. **21**(4): p. 198-206.
 133. Moylan, S., et al., *An Additive Manufacturing Test Artifact*. Journal of Research of the National Institute of Standards and Technology, 2014. **119**: p. 429-459.
 134. Moylan, S., *A Review of Test Artifacts for Additive Manufacturing*, in *NISTIR*. 2012.
 135. M, M., *Rapid prototyping and manufacturing benchmarking*. 2004, National University of Singapore.
 136. Rebaioli, L. and I. Fassi, *A review on benchmark artifacts for evaluating the geometrical performance of additive manufacturing processes*. International Journal of Advanced Manufacturing Technology, 2017. **93**(5-8): p. 2571-2598.
 137. Zhou, J.G., D. Herscovici, and C.C. Chen, *Parametric process optimization to improve the accuracy of rapid prototyped stereolithography parts*. International Journal of Machine Tools & Manufacture, 2000. **40**(3): p. 363-379.
 138. Campanelli, S.L., et al., *Statistical analysis of the stereolithographic process to improve the accuracy*. Computer-Aided Design, 2007. **39**(1): p. 80-86.
 139. Mahesh, M., et al., *A six-sigma approach for benchmarking of RP&M processes*. International Journal of Advanced Manufacturing Technology, 2006. **31**(3-4): p. 374-387.
 140. Lanzotti, A., et al., *On the Geometric Accuracy of RepRap Open-Source Three-Dimensional Printer*. Journal of Mechanical Design, 2015. **137**(10).
 141. Cruz Sanchez, F.A., et al., *Towards a standard experimental protocol for open source additive manufacturing*. Virtual and Physical Prototyping, 2014. **9**(3): p. 151-167.
 142. Pennington, R.C., N.L. Hoekstra, and J.L. Newcomer, *Significant factors in the dimensional accuracy of fused deposition modelling*. Proceedings of the Institution of Mechanical Engineers Part E-Journal of Process Mechanical Engineering, 2005. **219**(E1): p. 89-92.
 143. Abu Bakar, N.S., M.R. Alkahari, and H. Boejang, *Analysis on fused deposition modelling performance*. Journal of Zhejiang University-Science A, 2010. **11**(12): p. 972-977.
 144. Meisel, N. and C. Williams, *An Investigation of Key Design for Additive Manufacturing Constraints in Multimaterial Three-Dimensional Printing*. Journal of Mechanical Design, 2015. **137**(11).
-

145. Shi, Y., et al., *Manufacturability analysis for additive manufacturing using a novel feature recognition technique*. Computer-Aided Design and Applications, 2018. **15**(6): p. 941-952.
 146. Rupal, B.S., R. Ahmad, and A.J. Qureshi, *Feature-Based Methodology for Design of Geometric Benchmark Test Artifacts for Additive Manufacturing Processes*. 28th Cirp Design Conference 2018, 2018. **70**: p. 84-89.
 147. Qin, J., et al., *Research and application of machine learning for additive manufacturing*. Additive Manufacturing, 2022. **52**.
 148. Nag, S., et al., *Probabilistic Machine Learning Assisted Feature-Based Qualification of DED Ti64*. Jom, 2021. **73**(10): p. 3064-3081.
 149. El Kashouty, M.F., A.E.W. Rennie, and M. Ghazy, *A Novel Feature-Based Manufacturability Assessment System for Evaluating Selective Laser Melting and Subtractive Manufacturing Injection Moulding Tool Inserts*. Designs, 2023. **7**(3): p. 68.
 150. Gu, G.X., et al., *Bioinspired hierarchical composite design using machine learning: simulation, additive manufacturing, and experiment*. Materials Horizons, 2018. **5**(5): p. 939-945.
-